Geophysical Journal International

Geophys. J. Int. (2013) doi: 10.1093/gji/ggt024

Geophysical Journal International Advance Access published February 19, 2013

The stress field in Europe: optimal orientations with confidence limits

M. M. C. Carafa[1] and S. Barba[2]

[1]*Istituto Nazionale di Geofisica e Vulcanologia, Sezione di Sismologia e Tettonofisica, L'Aquila, Italy. E-mail: michele.carafa@ingv.it*
[2]*Istituto Nazionale di Geofisica e Vulcanologia, Sezione di Sismologia e Tettonofisica, Rome, Italy. E-mail: salvatore.barba@ingv.it*

Accepted 2013 January 21. Received 2013 January 16; in original form 2012 August 30

SUMMARY

In this study, we modify and extend a data analysis technique to determine the stress orientations between data clusters by adding an additional constraint governing the probability algorithm. We apply this technique to produce a map of the maximum horizontal compressive stress (S_{Hmax}) orientations in the greater European region (including Europe, Turkey and Mediterranean Africa). Using the World Stress Map data set release 2008, we obtain analytical probability distributions of the directional differences as a function of the angular distance, θ. We then multiply the probability distributions that are based on pre-averaged data within $\theta < 3^\circ$ of the interpolation point and determine the maximum likelihood estimate of the S_{Hmax} orientation. At a given distance, the probability of obtaining a particular discrepancy decreases exponentially with discrepancy. By exploiting this feature observed in the World Stress Map release 2008 data set, we increase the robustness of our S_{Hmax} determinations. For a reliable determination of the most likely S_{Hmax} orientation, we require that 90 per cent confidence limits be less than $\pm 60^\circ$ and a minimum of three clusters, which is achieved for 57 per cent of the study area, with uncertainties of less than $\pm 30^\circ$ for 19 per cent of the area. When the data density exceeds 0.8×10^{-3} data km^{-2}, our method provides a means of reproducing significant local patterns in the stress field. Several mountain ranges in the Mediterranean display 90° changes in the S_{Hmax} orientation from their crests (which often experience normal faulting) and their foothills (which often experience thrust faulting). This pattern constrains the tectonic stresses to a magnitude similar to that of the topographic stresses.

Key words: Plate motions; Seismicity and tectonics; Intraplate processes; Dynamics: gravity and tectonics; Neotectonics; Fractures and fault.

1 INTRODUCTION

This study aims to exploit the high data density of the World Stress Map release 2008 (hereinafter, WSM08; Heidbach *et al.* 2008) in the greater European region (including Europe, Turkey and Mediterranean Africa) to gain additional information on short-wavelength stress sources. Knowledge of the local stress field helps to identify potential slip on pre-existing favourably oriented fault planes (e.g. Sibson *et al.* 2011; Syracuse *et al.* 2012) and has an impact on seismic hazard assessment, geodynamics, hydrocarbon exploitation and global-to-regional–scale tectonics (Carafa & Barba 2011; Hergert & Heidbach 2011; Ghisetti & Sibson 2012). However, interpolating or smoothing the stress orientations of clustered and scattered data requires several assumptions and approximations.

Rebai *et al.* (1992) studied the irregular spatial distribution of stress data by determining the maximum horizontal compressive stress (S_{Hmax}) orientations on an irregular triangular element grid with the locations of grid nodes dependent upon the spatial distribution of the data. For clusters, the nodes were collocated at the centre, whereas for sparse data, the nodes were placed at data locations. At each node, Rebai *et al.* (1992) computed an average S_{Hmax} orientation by smoothing the S_{Hmax} data within a specified distance from the node. This distance was assumed to be proportional to the size of the smallest triangle connected to the node. The S_{Hmax} average was weighted by the quality factor assigned to the stress datum and by the scale factor associated with the type of S_{Hmax} indicator (decimetres to metres for borehole breakouts, kilometres for focal mechanisms). Within the triangular elements, the nodal values were linearly interpolated.

Lee & Angelier (1994) reconstructed the 2-D regional principal palaeostress axis orientations using two different approaches. In the first approach, the stress orientations were represented by a polynomial function of flat-Earth coordinates. The coefficients of the polynomial were determined using weighted least-squares to fit the measured S_{Hmax} orientations, with the weight of each S_{Hmax} datum dependent upon its uncertainty. In the second approach, the S_{Hmax} data were also weighted by a power-law function of the distance. The second approach provided better results, indicating that proper distance weighting is essential in stress interpolation.

Coblentz & Richardson (1995) quantified long-wavelength trends in the global S_{Hmax} orientations and stress regime patterns using the World Stress Map database release 1992 (hereinafter, WSM92; Zoback 1992). The authors binned the S_{Hmax} data into 582 $5^\circ \times 5^\circ$ cells. Of the 382 bins containing at least two S_{Hmax} orientations, Coblentz & Richardson (1995) estimated which bins had non-random S_{Hmax} orientations with standard deviation $<25^\circ$ by employing a Rayleigh test at the 90, 95 and 97.5 per cent confidence levels. The test assumes that random S_{Hmax} orientations follow a von Mises normal distribution (Mardia 1972). The hypothesis that stress orientations are random in WSM92 was rejected at the 97.5 per cent confidence level for 197 of 382 bins, suggesting that large portions of intra-plate regions have coherent S_{Hmax} orientations and are primarily in a state of compression.

Assuming two-point conditional probabilities, Bird & Li (1996) empirically determined the probability distributions of the angular differences (also called discrepancies) in the S_{Hmax} orientations based on WSM92 data. They used two approaches: one that accounted for the quality factor and one in which the clustered data were pre-averaged. Although both concepts are important, they have not yet been implemented simultaneously. Neglecting the quality factor results in the underweighting of the most accurate data, whereas when clustered data are used, the uneven data sampling causes a loss of precision that is not easily included in the error estimates.

Müller *et al.* (2003) determined the S_{Hmax} orientations using the nearest-neighbour regression method. The authors compared two approaches using either a fixed search radius or a fixed number of nearest neighbours. The smoothing was performed at grid points, with the data weighted by both quality and distance. In particular, the quality weight was 1 for rank A, 0.75 for rank B, 0.5 for rank C and 0 for ranks D and E (see Zoback (1992) for a description of the quality factors). The distance weight was expressed as a tricube weight function:

$$w(x, x_i) = \begin{cases} \left[1 - \left(\frac{\|x - x_i\|}{R}\right)^3\right]^3 & \text{for} \quad \| x - x_i \| < R \\ 0 & \text{otherwise} \end{cases},$$

where x_i is the position of the ith data point and R is either the fixed search radius or the distance to the $(N + 1)$th nearest neighbour. Müller *et al.* (2003) performed checkerboard-like synthetic tests and verified that using a fixed search radius is preferable for recovering the stress domains. To avoid interpolating stress orientations in areas of poor data coverage, minimum threshold values for the sum of the quality and distance weights were suggested. The approach of Müller *et al.* (2003) proved to be flexible and capable of providing an empirical model of the stress processes. However, this approach is sensitive to outliers and suffers when the data density is low.

Rather than using discrete weights, several groups (e.g. Hardebeck & Michael 2006; Arnold & Townend 2007) have developed methods to propagate observational errors as formal uncertainties in S_{Hmax}, which comprise mainly focal mechanisms. Hardebeck & Michael (2006) used a damped inversion method to determine stress on a grid, which minimises the difference between adjacent points. The damped inversion removes the stress rotation artefacts exhibited by undamped inversions and resolves stress rotations better than moving-window approaches. Arnold & Townend (2009) developed a Bayesian formulation for estimating tectonic stress orientations, which combines a geologically based prior stress model and focal mechanism observations, including their precisions. Their technique produces the posterior density function of the principal components of the stress tensor and of the stress-magnitude ratio, which have been used to determine S_{Hmax} following the approach of Lund & Townend (2007).

Heidbach *et al.* (2010) calculated the global S_{Hmax} orientations by smoothing stress data that were weighted by both quality and distance. The distance weighting function was min $(1/D, 1/20$ km), where D is the distance between the data location and grid point and min represents the minimum of the two arguments. The quality weights were 1/15, 1/20 and 1/25 for A-, B- and C-quality data, respectively. The S_{Hmax} orientations were defined if there were at least five WSM08 data within the variable search radius and if the weighted standard deviation was $\leq 25^\circ$. Pierdominici & Heidbach (2012) introduced an additional condition that the data be located in two diagonal quadrants, with at least 10 WSM08 data within the search radius. No constraints were placed on the standard deviation in their study.

In this paper, we aim to address three major issues that have not previously been resolved simultaneously: the scatter in S_{Hmax} orientations, the uneven sampling of stress data, and the correlation of stress orientations with distance. We modified and extended the clustered data analysis technique used by Bird & Li (1996) by adding a constraint governing the probability algorithm for estimating S_{Hmax} orientations. Given the intrinsically clustered nature of earthquakes and the uneven sampling of boreholes, we pre-averaged clustered data and updated the empirical probability distributions using the WSM08. In agreement with the data, we modelled the probabilities as exponentially decreasing with discrepancy, thereby compensating for the low data density. An S_{Hmax} orientation was assigned to each interpolation point if three conditions were satisfied: (i) a minimum of three clusters; (ii) 90 per cent confidence limits less than $\pm 60^\circ$ and (iii) a maximum search radius of 327 km.

The resulting stress maps have 90 per cent confidence limits of less than $\pm 45^\circ$ for 38 per cent of the study area and uncertainties of less than $\pm 30^\circ$ for the 19 per cent. The results presented in this work cover 57 per cent of the entire study area. Our S_{Hmax} orientations overlap with 28 per cent of those in Heidbach *et al.* (2010); the spatial distributions of the two stress fields are therefore complementary. Where the two maps overlap, the results differ by more than 30° for only 2 per cent of our study area. The stress orientations determined using our method are generally consistent with the S_{Hmax} orientations obtained using geological indicators, earthquakes and numerical models. Our method is able to detect several small-scale (20–50 km) stress perturbations, thereby better constraining and complementing the stress field determinations available elsewhere in the literature.

2 DATA AND METHOD

Based on previous studies of stress interpolation, the angular differences (discrepancies) between two S_{Hmax} orientations tend to increase with distance or, alternatively, the closest S_{Hmax} datum to an interpolation point is weighted most heavily. Of the various data weighting algorithms suggested in the literature, we adopted the approach of Bird & Li (1996). In this approach, S_{Hmax} is determined at each integration point using two-point conditional probabilities and assuming all of the WMS08 data to be independent. The conditional probability of an event is the probability of that event occurring given that another event has already occurred. In terms of conditional probabilities, the S_{Hmax} orientation represents the azimuth with the highest probability of occurring given the neighbouring WSM08 data. We defined the empirical two-point conditional probability based on the stress data (see Section 2.1) and the analytical

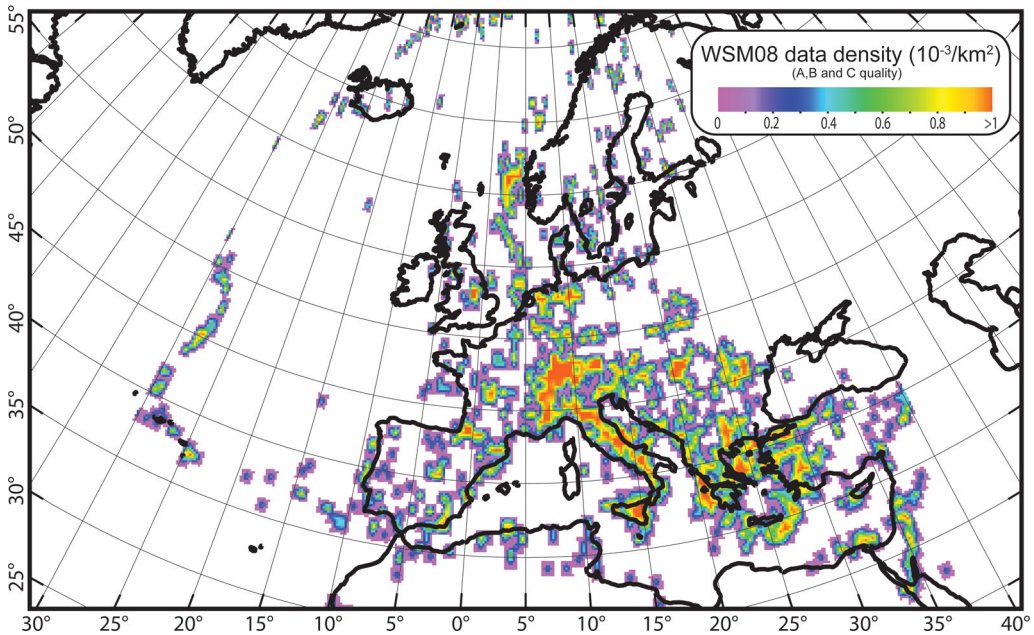

Figure 1. WSM08 data density in Europe. Densities were computed for 0.5° × 0.5° cells, from 25N to 76N latitude and 30W to 40E longitude. Cells with no data entries are not coloured.

probability using least-squares fitting (Section 2.2). We then used the declustering method of Bird & Li (1996) and the analytical probabilities to determine the S_{Hmax} orientations. We applied our method to study short-wavelength patterns over a wide area (total extent of 2.7×10^9 km^2) from 30W to 40E longitude and 25N to 76N latitude, roughly corresponding to the geographic location of the greater European region.

2.1 Data

We used the S_{Hmax} data records from the WSM08 data set (http://www.world-stress-map.org). Each stress datum was assigned a quality factor between A and E, with A being the highest quality and E the lowest. The standard deviations of A-, B-, C- and D-quality data records are within ±15°, ±20°, ±25° and ±40°, respectively. E-quality data records have standard deviations greater than 40°. The WSM08 data set consists of 21 750 data records, of which 16 961 have qualities of A–C; these data form approximately 1.4×10^8 unique pairs, representing a significant improvement over the 1.8×10^7 data pairs obtained by Bird & Li (1996) using WSM92. The data density increased from 0.012×10^{-3} data km^{-2} in WSM92 to 0.041×10^{-3} data km^{-2} (0.033×10^{-3} data km^{-2} for A-, B- and C-quality data) in WSM08. North America, Europe and China are the most densely sampled zones. Within Europe, Italy and Switzerland have the highest data densities, with an average of 3×10^{-3} data km^{-2} (Fig. 1). However, many locations in Anatolia, the Hellenic Arc, the Pyrenees, Northwestern Europe and the North Sea have densities exceeding 0.7×10^{-3} data km^{-2}.

2.2 Empirical probabilities

The angle between any pair (r, s) of S_{Hmax} data points on Earth is the discrepancy β defined by Bird & Li (1996) as follows:

$$\beta = \min_{m=-3}^{+3} |\alpha_{\mathrm{r}} - \gamma_{\mathrm{r}} + \gamma_{\mathrm{s}} - \alpha_{\mathrm{s}} + m \times 180^\circ|, \tag{1}$$

where m is an integer between −3 and 3, γ_{r} and γ_{s} are the local azimuths of the great circle connecting the two data points, and α_{r} and α_{s} are the S_{Hmax} azimuths relative to north (Fig. 2). Our first step was to determine the number of WSM08 pairs as a function of the discrepancy β and range (or angular distance) θ. Following Bird & Li (1996), we used 30 3°-wide sectors for β and 150 concentric annuli for θ. The annulus n is defined such that $\theta_{n-1} \leq \theta < \theta_n$, with

$$\theta_n \cong \cos^{-1}\left\{1 - 2\,(n/150)^{1/(1-\varepsilon)}\right\}. \tag{2}$$

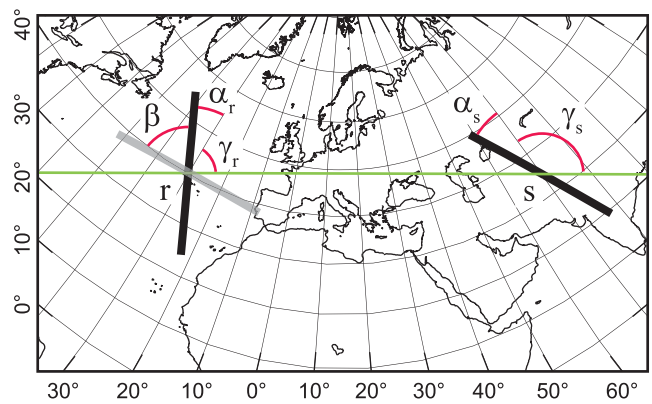

Figure 2. Cartographic description of the discrepancy angle β. For each pair of stress data points, r and s, we define the great circle (green line) between r and s for an oblique Mercator projection. The discrepancy is the angle between the two S_{Hmax} orientations as expressed in eq. (1). The S_{Hmax} orientations of r and s are shown in black, and the S_{Hmax} orientation of s, translated onto r, is shown in grey.

The WSM08 data set is 3.5 times larger than the WSM92 data set available to Bird & Li (1996) (6000 data points), for which they used $\varepsilon = 0.4$. The larger data set can be exploited by increasing either the number of discrepancy bins (e.g. using a finer binning for β) or the number of annuli at short range (i.e. $\varepsilon > 0.4$). Based on a series of tests, we chose the latter option. We selected $\varepsilon = 0.6$, which enabled the investigation of short ranges while avoiding high uncertainties for some S_{Hmax} orientations.

We used 150 annuli for the range θ and 30 3°-wide sectors for the discrepancy angle β, resulting in a total of 4500 bins. Each bin was

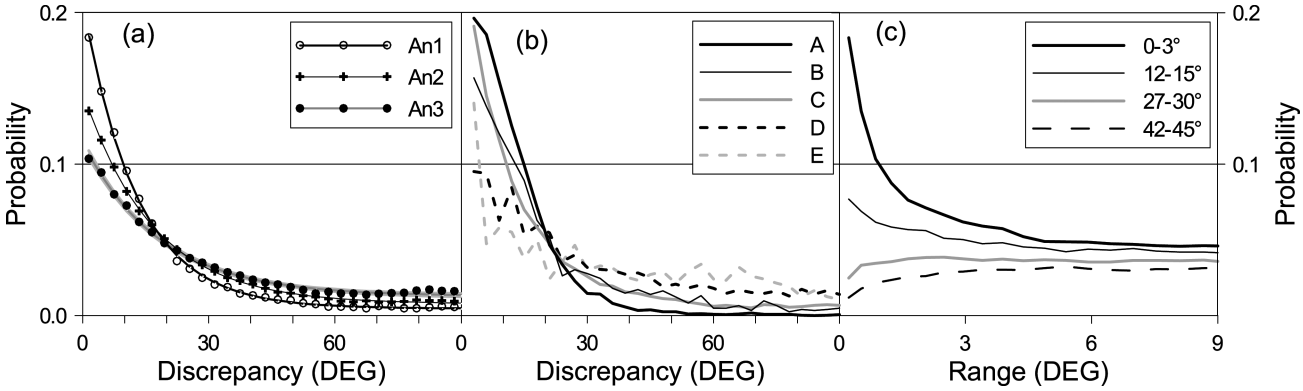

Figure 3. Probability distributions as a function of discrepancy and range. (a) Analytical (lines) and empirical (symbols) probabilities for Annuli (An) 1–3 (A–C quality factors); (b) empirical probabilities for Annulus 1 for A-E quality factors; (c) empirical probabilities for various discrepancy intervals. The lines connect the empirical values in (b) and (c).

identified by two indices, $n(\theta)$ and $i(\beta)$, such that the range angle θ lies within the bounds $\theta_{n-1} \leq \theta \leq \theta_n$ and the index i is given by $i = \frac{\beta}{3^\circ} + 1$, rounded down to the nearest integer. The number of data pairs within each bin can be represented by a matrix $C_{i(\beta),n(\theta)}$ of integers.

The probability that a discrepancy β at range θ falls into angular bin i is given by

$$D_{i(\beta),n(\theta)} = \frac{C_{i(\beta),n(\theta)}}{\sum_{j=1}^{30} C_{j,n(\theta)}}. \tag{3}$$

Given a datum r with azimuth α_r, we can define the two-point conditional probability $P[k(\alpha_r)|\alpha_s]$ for any azimuth α_s at any range angle θ determined by the appropriate angular bin k $(0 \leq \alpha < 180; k = 1 \cdots 60)$

$$P[k(\alpha_r)|\alpha_s] = \frac{1}{2} D_{i(\beta),n(\theta)}, \tag{4}$$

where the factor of $1/2$ avoids the double counting of pairs (there are two possible azimuths for the same β value for each data pair).

Fig. 3(a) supports our choice of ε for the investigation of short ranges. The probabilities decrease sharply for the first three annuli with $\varepsilon = 0.6$, whereas smaller values of ε fail to capture this probability variation, resulting in a uniform probability distribution. For example, with $\varepsilon = 0.4$, Annulus 1 contains the upper limit set to 1.76°, whereas for $\varepsilon = 0.6$, this upper limit falls in Annulus 6. Due to the increased number of data points in WSM08 compared to the WSM92 data set, the finite sample effect for each bin was on the order of 2 per cent, similar to the value found by Bird & Li (1996) in their analysis of the WSM92 data set.

We divided the WSM08 data set into five classes according to the quality factor that was assigned to each data record. The probability distributions were of comparable width for the A-, B- and C-classes (Fig. 3b) and substantially narrower than for the D- and E-classes for all ranges. The D- and E-quality data exhibited a large scatter in the probability distribution at short ranges, indicating a lack of correlation. We therefore discarded the 3946 data records with D- or E-quality factors and considered only WSM08 data with A-, B- or C-quality factors in our analysis.

The high probability of finding small discrepancies at short ranges ($\theta \cong 0^\circ$) does not exclude local scatter, as illustrated in Fig. 3(c) by the non-zero probabilities of high discrepancies in β. These discrepancies are related to the repeatability of the measurements, depth variability, or heterogeneities in the material properties. Following the approach of Barba *et al.* (2010), we estimated the repeatability error at zero distance $\sigma_0 = \sigma\,(0)$ by interpolating the standard deviation σ versus the range θ using the following equation:

$$\sigma\,(\theta) = a + b\theta + c\theta^{0.5}. \tag{5}$$

The error was $\sigma_0 = 4^\circ \pm 1^\circ$ for A-quality data (Fig. 4a), $\sigma_0 = 10.9^\circ \pm 0.6^\circ$ for B-quality data, and $\sigma_0 = 13.2^\circ \pm 0.7^\circ$ for C-quality data. Combining the A-, B- and C-quality data yields $\sigma_0 = 11.8^\circ \pm 0.5^\circ$ (Fig. 4a).

The inclusion of D-quality data would worsen the results, given the large scatter in the probability distributions for all discrepancies (Fig. 3b). The results are affected by both the larger uncertainties for small discrepancies in D-quality data and the larger biases for larger discrepancies. An alternative is weighting the A-, B- and C-quality data proportionally to the error σ_0 (eq. 5), which essentially gives a higher weight to A-quality data. Although formally correct (Arnold & Townend 2007), given the relatively low number of A-quality data compared to B- and C-quality data, the different weighting would have a negligible effect on the results while making the procedure more complex. However, this point may be reconsidered in the future when a greater number of A-quality data are available.

For $\theta < 3^\circ$, the correlation between data pairs is high and the probabilities of large discrepancies are small, whereas for $\theta > 6^\circ$, the discrepancy probabilities do not show any significant trends (Fig. 3c). Following Bird & Li (1996), we define a scalar measure of the correlation as follows:

$$I_{\mathrm{cor}}(\mathrm{WSM08}) = \frac{\sum_{i=1}^{10} D_i}{\sum_{j=21}^{30} D_j}, \tag{6}$$

that is, the ratio of D (eq. 3) for 'small' discrepancies ($0 < \beta \leq 30^\circ$) to D with 'large' discrepancies ($60^\circ < \beta \leq 90^\circ$). Bird & Li (1996) reported a quasi-exponential falloff of I_{cor}(WSM92) out to a range of 22°, whereas I_{cor}(WSM08) exhibited a quasi-exponential decrease for all ranges (Fig. 4b). To improve the detail at short range, we used the empirical probabilities for $\theta < 3^\circ$ (Annuli 1–8) instead of $\theta < 22^\circ$, as adopted by Bird & Li (1996). The choice of the upper value of θ depends on the complexity of the study region. For example, compared to the Pacific Basin in the Tertiary period, the Mediterranean/Tethyan Basin is of similar complexity and has a similar number of subduction zones, yet much shorter along-strike distances. Therefore, the stress fields associated with subduction, mountain ranges and perhaps hanging slabs in the Mediterranean have relatively short length scales compared to those of the Pacific

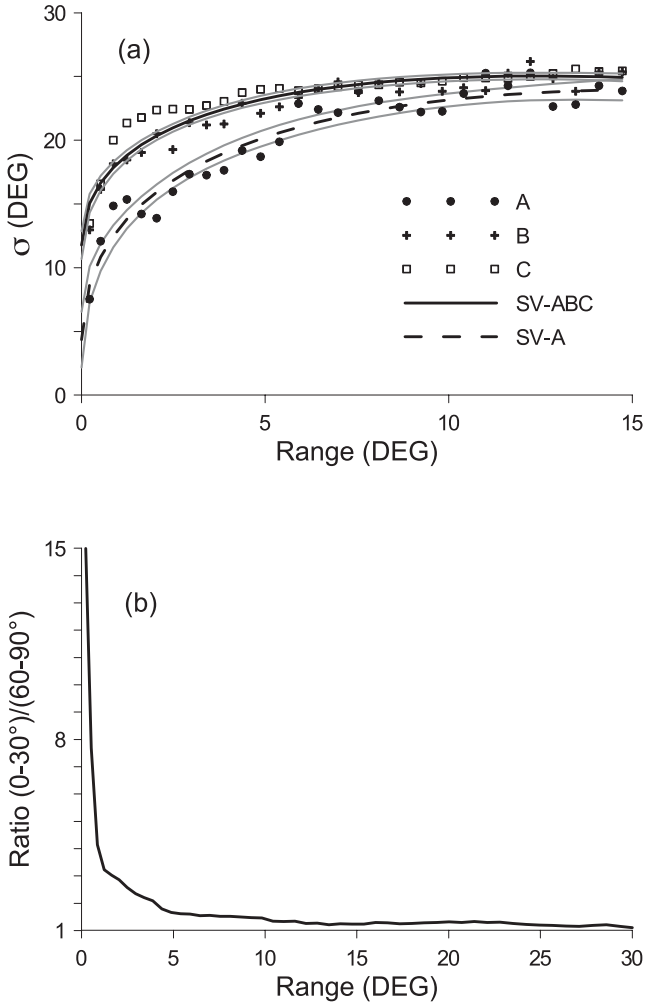

Figure 4. (a) Standard deviation versus range (symbols) and analytical representation of eq. (5) (SV: lines, with confidence limits); (b) the ratio of D (eq. 3) for 'small' discrepancies ($0 < \beta \leq 30°$) to "large" discrepancies ($60° < \beta \leq 90°$) versus range.

stress fields. Thus, using lower cut-off values than those used in global modelling allows the resolution of these smaller features.

The exponential trend of the probabilities confirms the hypothesis of Bird & Li (1996) that the "correlation horizon" at a range of $\theta = 22°$ is due to uneven sampling of Earth in WSM92. The decreased ringing in I_{cor}(WSM08) with respect to I_{cor}(WSM92) is due to the eightfold increase in the number of unique pairs in WSM08.

2.3 Analytic probabilities and interpolation method

The probability distributions (Fig. 3a) follow an exponential law for all annuli. If few data are considered, the probabilities do not behave exponentially, which explains why this behaviour has not been observed previously. Based on highly successful regressions ($R^2 \geq 0.99$), we parameterised the empirical probabilities of eq. (4) as follows:

$$P^*[k(\alpha_{\mathrm{r}})|\alpha_{\mathrm{s}}] \equiv P^*(k_{\mathrm{r}}|s) = P_0^* + P_1^* \exp(-\theta/\theta_0), \tag{7}$$

where P^* denotes the analytic probability and θ_0, P_0^* and P_1^* are constants determined from a non-linear least-squares fit to the empirical probabilities P (eq. 4) within the annulus. In this equation, we simplified the notation by using the integer indices r and s in place of the azimuths α_{r} and α_{s}. The values of θ_0, P_0^* and P_1^* for Annuli 1–8 are listed in Table 1.

Let x be a point at which we wish to estimate the stress orientation, and let us select the WSM08 data points within a range of θ_n (eq. 2). The probability of the azimuth at x falling into bin k given one datum r is $P^*(k_x|r)$ (eq. 7). Although the presence of independent data is easily formalised through probability multiplication, clustered data require further analysis. A pair of stress data points r and s form a cluster if

$$P^*(s|r) > \max_{i=r,s} P^*(i|x), \tag{8}$$

that is, the two-point conditional probability of r and s is larger than the highest possible conditional probability with respect to the interpolation point x. The opposite guarantees that the data are independent. Note that this definition of independence depends on distance; a pair of data points can both be independent for interpolation points located between the data and form a cluster when they are far away from the interpolation point. After the clusters have been defined, a two-pass procedure is applied. In the first pass, the clustered data are pre-averaged, resulting in a set of fully independent S_{Hmax} orientations. This set consists of pre-averaged data and data points determined to be independent according to eq. (8). In the second pass, the S_{Hmax} orientation is interpolated to x.

The pre-averaged values of the clustered data are obtained in the first pass using the two-point conditional probability distributions, assuming no azimuthal dependence between the data. For simplicity, we omit the cluster index. The S_{Hmax} orientation of the cluster is assigned to its geographical centre, hereinafter denoted by z, and is determined using the maximum likelihood method. For each trial azimuth, defined by an integer value of k_z ($k_z = 1, \ldots, 60$ with 3° bins), we compute the probability as

$$P_N^*(k_z) = \frac{\prod_{i=1}^{N} P^*(k_z|i)}{\sum_{j=1}^{60} \prod_{i=1}^{N} P^*(j_z|i)}, \tag{9}$$

Table 1. Regression parameters and related standard error of eq. (7) for Annuli 1 to 8. P_0^*, P_1^* and θ_0: coefficients of eq. (7) considering the associated standard errors. RMS: root mean square between empirical and analytical probabilities. R^2: coefficient of determination, which measures the goodness of the regression fit.

Annulus	$P_0^* \times 10^{-3}$	St. error $P_0^* \times 10^{-3}$	$P_1^* \times 10^{-3}$	St. error $P_1^* \times 10^{-3}$	θ_0 (°)	St. error θ_0 (°)	RMS (10^{-3})	R^2
1	4.6	0.4	204	1	12.7	0.1	1.3	0.999
2	7.6	0.3	140.5	0.7	16.6	0.2	0.8	0.999
3	12.7	0.6	102	1	18.4	0.5	1.6	0.996
4	14.9	0.8	81	1	20.7	0.9	1.8	0.993
5	14.2	0.9	70	1	25	1	1.7	0.991
6	14	1	65	1	28	2	1.8	0.989
7	13.8	0.9	57.1	0.8	33	2	1.1	0.995
8	14.8	0.8	51.4	0.7	35	2	0.8	0.996

Table 2. Percentage of the area in which the stress orientations can be recovered for various threshold values of $\Delta\alpha$ and N_C, with the maximum search radius set to the upper limit of Annulus 8 ($\theta_8 < 2.94^\circ$; 327 km). The total extent of the study area is 2.71×10^9 km^2.

Minimum number of clusters (N_C)	Maximum value of 90 per cent confidence interval $\Delta\alpha$			
	20°	40°	60°	80°
1	18 per cent	44 per cent	59 per cent	75 per cent
3	18 per cent	44 per cent	57 per cent	63 per cent
5	18 per cent	43 per cent	52 per cent	56 per cent
7	18 per cent	40 per cent	46 per cent	49 per cent

where N is the number of stress data forming the cluster. The maximum-likelihood estimate of the S_{Hmax} orientation at the cluster centre z is $\alpha_z = \left(k_z - \frac{1}{2}\right) 3^\circ$, where k_z is the integer that maximises $P_N^*(k_z)$. This operation is performed for each cluster.

In the second pass, the S_{Hmax} orientations are interpolated to x. To identify the now fully independent orientations, we call them 'clusters' and label them as c regardless of whether they arose from pre-averaging. For each trial azimuth, defined by an integer value of k_x ($k_x = 1, \ldots, 60$ with 3° bins), we calculate the probability as

$$P_{N_C}^*(k_x) = \frac{\prod_{c=1}^{N_C} P^*(k_x|c)}{\sum_{j=1}^{60} \prod_{c=1}^{N_c} P^*(j_x|c)}, \tag{10}$$

where N_C is the number of clusters within range θ_n (eq. 2). However, the index n is omitted in eq. (10) for simplicity. The maximum likelihood estimate of the S_{Hmax} orientation at interpolation point x is

$$\alpha_x = \left(k_x - \frac{1}{2}\right) 3^\circ, \tag{11}$$

where k_x is the integer that maximises $P_{N_C}^*(k_x)$ in eq. (10). The 90 per cent confidence interval $\Delta\alpha$ is determined using the following equation:

$$\int_{\alpha_x - \Delta\alpha}^{\alpha_x + \Delta\alpha} p_N^*\left(\alpha_x' \bmod 180^\circ\right) \mathrm{d}\alpha_x' = 0.90, \tag{12}$$

where $p_N^*\left(\alpha_x' \bmod 180^\circ\right)$ is the functional form corresponding to the discrete $P_N^*(k_x)$ and 'mod' indicates the remainder of the integer division, used to account for the periodicity of α_x'. This procedure allows the uncertainties due to data scattering (shown in Fig. 3 and included in eq. 10) to propagate into the posterior uncertainties $\Delta\alpha$ (eq. 12).

We adopt two conditions to ensure a well-defined S_{Hmax} orientation: (i) $N_C \geq 3$ within a specified range θ_n and (ii) $\Delta\alpha \leq 60^\circ$ for the N_C clusters. The upper limit of the 90 per cent confidence interval ($\Delta\alpha \leq 60^\circ$, corresponding to $\sim 2\sigma$ in a normal distribution) accounts for the error associated with C qualities ($1\sigma = 30^\circ$), the most common quality factor in WSM08. The search began with Annulus 1 ($\theta_1 < 0.22^\circ$) and increased stepwise up to Annulus 8 ($\theta_8 < 3^\circ$). We selected the first annulus n (and thus the smallest range) that satisfied both conditions. However, if the conditions were not met by Annulus 8 (the upper limit), then we did not assign an S_{Hmax} orientation to the interpolation point x.

3 STRESS INTERPOLATION IN EUROPE

We interpolated the WSM08 S_{Hmax} orientations using data-driven analytical weight distributions after pre-averaging the clustered data in the area from 30W to 40E longitude and 25N to 76N latitude. We weighted by distance and discrepancy and adopted thresholds for the number of clusters N_C and the 90 per cent confidence limits $\pm\Delta\alpha$. The threshold values determine the interpolated stress orientations α_x (eq. 11) and limit the area in which the stress orientations can be recovered (Table 2). We illustrate our results with examples in Europe.

Stress orientations were determined for 57 per cent of the study area. The zones with the smallest $\Delta\alpha$ values are the Apennines, the Dinarides, the Alps, Western Turkey and the Aegean Sea. We found $\Delta\alpha < 15^\circ$ for 3 per cent of the study area, $\Delta\alpha < 30^\circ$ for 19 per cent of the area, and $\Delta\alpha < 45^\circ$ for 38 per cent of the area (Fig. 5). This fraction of recovered stress orientations is satisfactory and comparable to those obtained in other studies (e.g. Heidbach *et al.* 2010). The search radius was smaller than the upper limit of Annulus 3 ($\theta_3 < 0.86^\circ$, 96 km) for a large part of continental Europe and the Norwegian Sea (Fig. 6). Conversely, S_{Hmax} was not recovered in the Atlantic Ocean, Northern Africa, or Russia due to the scarcity of data in those locations. The S_{Hmax} orientations were interpolated using $3 \leq N_C \leq 4$ (average number of data $N = 4.87$) for 28 per cent of the study area, $5 \leq N_C \leq 8$ (average $N = 8.89$) for 22 per cent of the study area, $9 \leq N_C \leq 12$ (average $N = 16.05$) for 5 per cent of the study area, and $N_C > 12$ (average $N = 31.42$) for 2 per cent of the study area (Fig. 7). Due to the high density of uniform data, the stress orientations were calculated using large N_C values and short ranges in the Pyrenees, Central Italy and Romania. Large N_C values and long ranges were used in the Western North Sea, Tyrrenian Sea, Western Alps and Ionian Sea due to locally scattered WSM08 S_{Hmax} orientations. Our results are provided in both numeric and map form at a resolution of $0.1^\circ \times 0.1^\circ$ as an electronic supplement to this article (Table S1 and Fig. S1).

The S_{Hmax} map (Fig. S1, available in the auxiliary material) displays the same main features already described in the literature in relation to the European stress field (Müller *et al.* 1992; Gölke & Coblentz 1996). The stress pattern in Northwestern Europe (Fig. 8a) is dominated by long-wavelength features and follows the NW–SE pattern expected for a stress field produced by plate-scale forces (Müller *et al.* 1992, 1997; Gölke & Coblentz 1996). Therefore, plate boundary forces are likely the main factor controlling the stress orientation in Northwestern Europe (Goes *et al.* 2000). Scandinavia exhibits scattered stress orientations (Fig. 8b), likely due to a combination of plate boundary forces, glacial isostatic adjustment and local heterogeneities (Bungum *et al.* 2010). However, no clear radial pattern can be observed, indicating that rebound stresses are either spatially limited or of relatively low magnitude. The S_{Hmax} orientations in Iberia display substantial variability (Fig. 8c). The stress field has a complex pattern; first-order compressive stresses, such as the Atlantic ridge push and Eurasia–Africa convergence, interact with and are perturbed by local stress ffields, such as the rifting of the Valencia Trough and topographic loading (De Vicente *et al.* 1996; Andeweg *et al.* 1999; Liesa & Simón 2009).

In Italy (Fig. 8d), the NNW–SSE S_{Hmax} orientations mark the extension in the Apennines (Boncio & Lavecchia 2000; Carminati

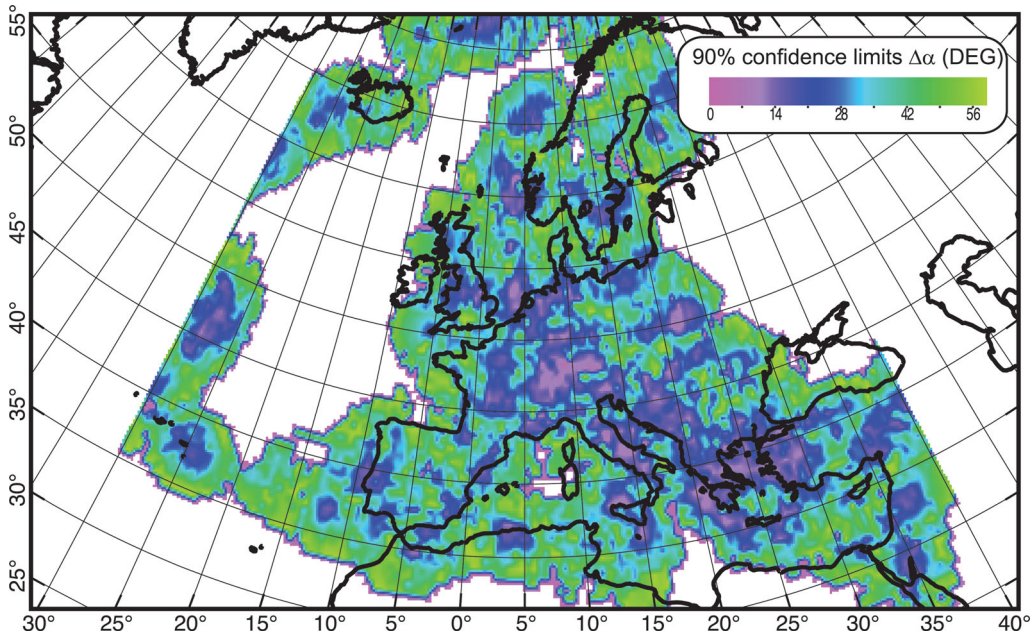

Figure 5. Colour-coded map of the 90 per cent confidence limits ($\pm\Delta\alpha$).

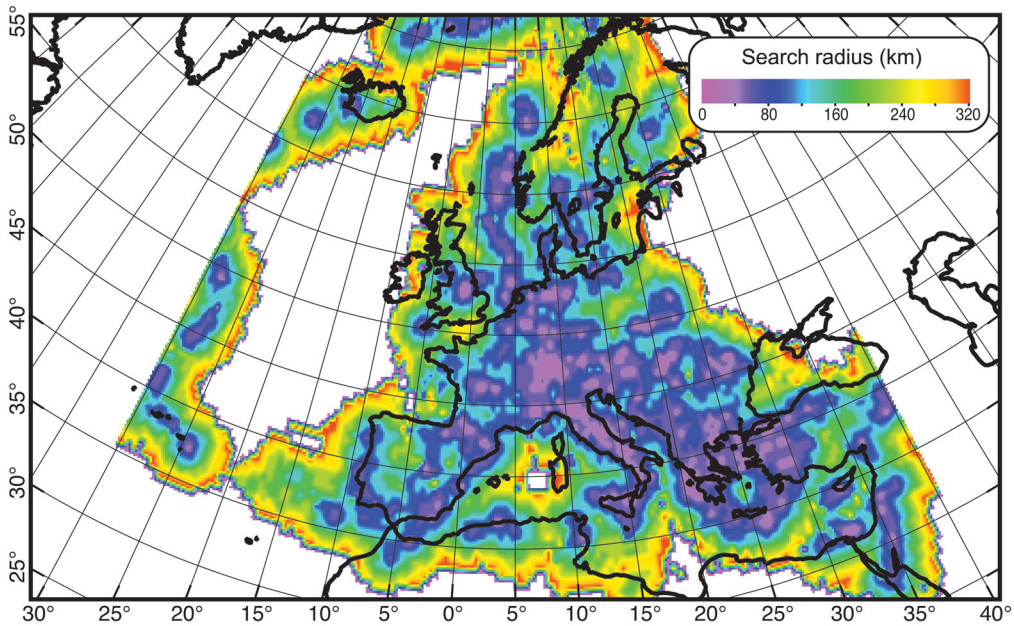

Figure 6. Minimum search radius for which $\Delta\alpha < 60^\circ$ and $N_C \geq 3$. The upper bound is set to $\theta = 2.94^\circ$.

et al. 2001; Barba *et al.* 2010), whereas the S_{Hmax} in the Adria microplate corresponds with the active Adria–Eurasia compression (Kastelic & Carafa 2012; Barba et al. 2013). The S_{Hmax} orientations in the Eastern Mediterranean rotate from NNW–SSE to NW–SE in the Marmara Sea and to E–W in the Northern Aegean Sea (Fig. 8e). This pattern follows the lateral extrusion of Anatolia and the N–S directed backarc spreading caused by the rollback of the Hellenic subduction zone (Taymaz *et al.* 1991; Hergert & Heidbach 2011; Petricca *et al.* 2013).

Short-wavelength features are scattered throughout the map of the interpolated S_{Hmax} orientations. Short-wavelength patterns typically arise from crustal heterogeneities, topographic effects and sharp variations in the kinematics; we describe a few examples associated with these different causes.

Crustal-scale local stress sources, such as lateral density contrasts, rifting processes and diapirism, interfere with regional stresses and can result in S_{Hmax} reorientation depending on the stress magnitudes and angular differences. Such a phenomenon occurs in Vrancea and the Southeastern Carpathians (Fig. 8e) and has been extensively studied by Müller *et al.* (2010), who inferred that the high variability in the stress orientations indicates that the stresses generated by local sources are of similar magnitude to the regional

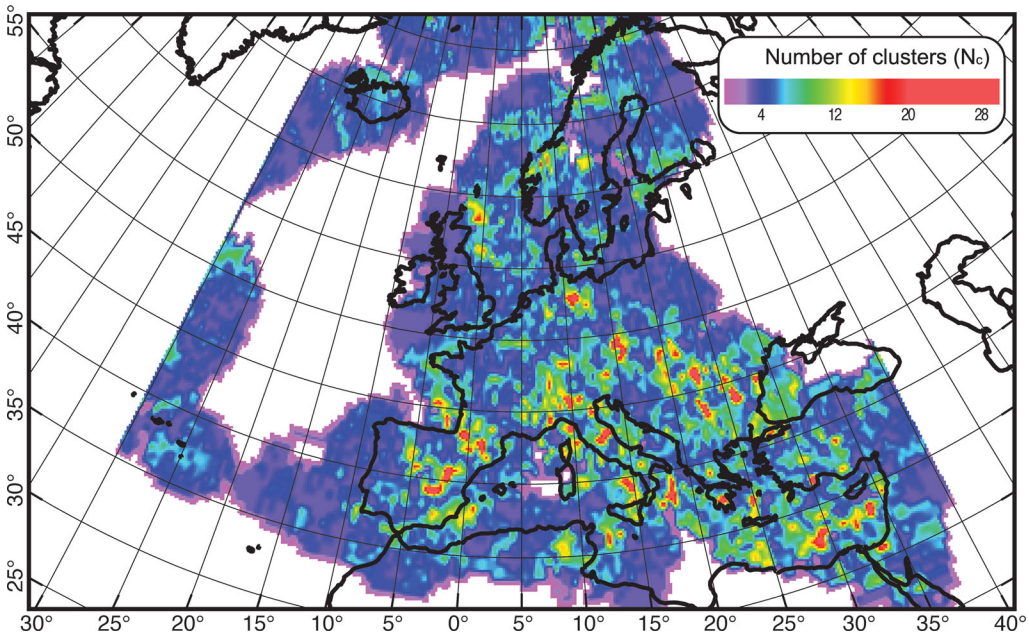

Figure 7. Number of clusters N_C used to interpolate S_{Hmax}.

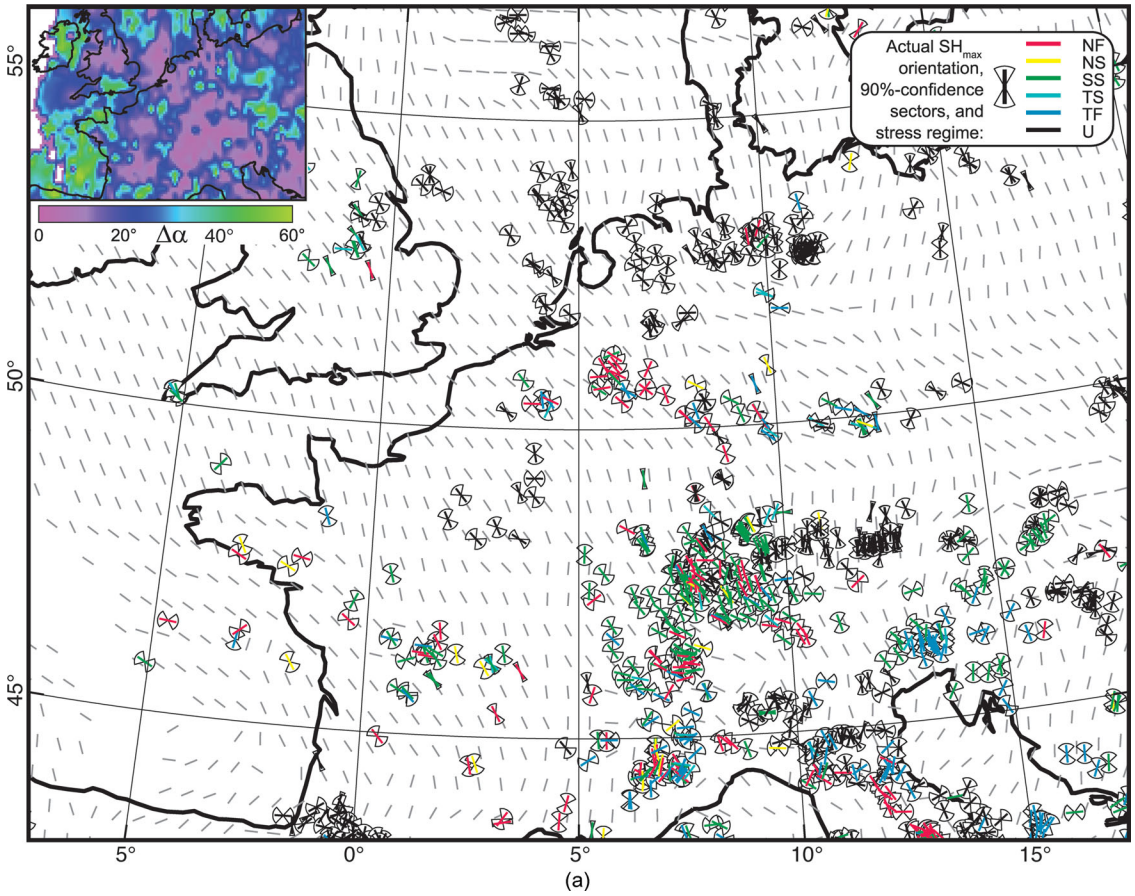

Figure 8. S_{Hmax} orientations in Europe. (a) Northwestern Europe; (b) Scandinavia; (c) Iberia; (d) Italy; (e) Southeastern Europe. Thick bars: WSM08 data; thin black bars: interpolated S_{Hmax} (this work). Inset: colour-coded map of the 90 per cent confidence limits ($\pm\Delta\alpha$).

stress. In the Central Adriatic (Fig. 8d), the S_{Hmax} orientations also arise from an interplay between the regional stresses, caused by the Adria-Eurasia collision (Kastelic & Carafa 2012), wrench tectonics and salt diapirism (Grandic & Markulin 2000; Geletti *et al.* 2008; Korbar 2009). A more extreme case is the easternmost part of the Po Plain, where S_{Hmax} takes on an E–W orientation (Fig. 8d), which is in contrast to the regional N–S compression, as determined from earthquakes and geodesy (Carminati & Vadacca 2010; Caporali

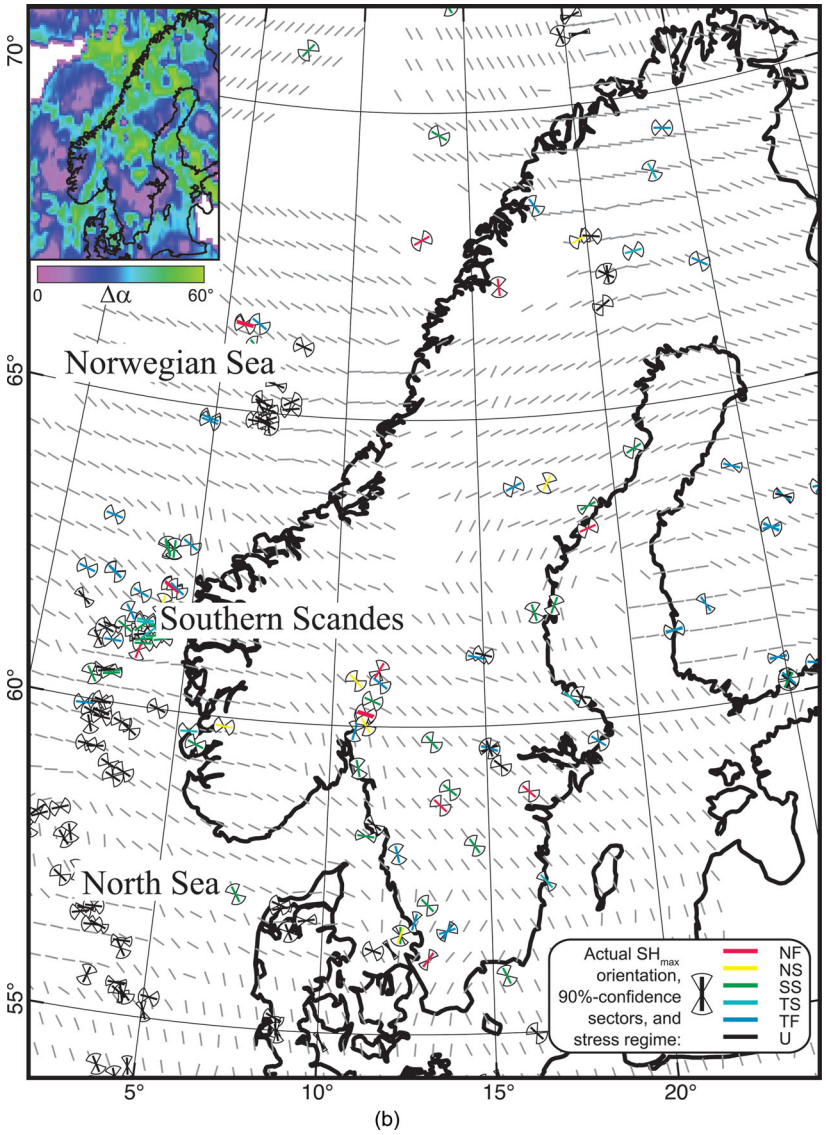

Figure 8. (*Continued.*)

et al. 2011). The smoothed orientations are instead determined using the WSM08 data closest to the interpolation point, which reflect the sedimentary infilling of the Po Plain. The rotation of these stress data with respect to the regional trend can be ascribed to differential sediment compaction, favoured by the presence of anticlines and large variations in the sediment thickness. The shallow E–W orientations of S_{Hmax} due to the tensional, strike-slip stress field at a depth of approximately 1200 m are perpendicular to the deeper N–S orientations of S_{Hmax} due to the compressive stress field near the main detachment (Carminati *et al.* 2010). In this specific case, the three closest data points are iso-oriented and represent the sediments, and our algorithm captures the local and shallow tensional stress field induced by the differential sediment compaction. However, applying our algorithm to a different data set (e.g. the regional moment tensors calculated using the method of Herrmann *et al.* 2011) yields N–S S_{Hmax} orientations.

In the case of topographically induced stress, S_{Hmax} can align with a mountain chain at the highest elevations and rotate perpendicularly to the chain at the foot of the belt (Assameur & Mareschal 1995; Carminati *et al.* 2004). This short-wavelength pattern is evident in the interpolated stress map for the Pyrenean domain (Fig. 8c) and the Eastern and Western Alps (Fig. 8d). However, the pattern is less evident in the Southern Scandes (Fig. 8b) due to the relative scarcity of data there. Parallel trends in S_{Hmax} and the isohypses are typically interpreted as the spreading of topographical crests at high elevation in mountains and as gravitational collapse at mountain bases (Decker *et al.* 1993; Herraiz *et al.* 2000; Sue *et al.* 2007; Pascal & Cloetingh 2009; Bungum *et al.* 2010). In Southern Cyprus, S_{Hmax} follows a N–S orientation (Fig. 8d), supporting the presence of a relatively small collision zone between Cyprus and the Eratosthenes Seamount, which is a faulted block that has been uplifted by 1500 m. Cyprus and its surroundings are characterised by NE–SW S_{Hmax} orientations (Fig. 8e) that correspond to the collision between Sinai and Anatolia (Wdowinski *et al.* 2006).

Another observed short-wavelength feature is the sudden change in tectonic style. Moving from extension to compression implies a rotation of the stress tensor and a consequent sudden reorientation of S_{Hmax}. This phenomenon is observed in the Northern Apennines

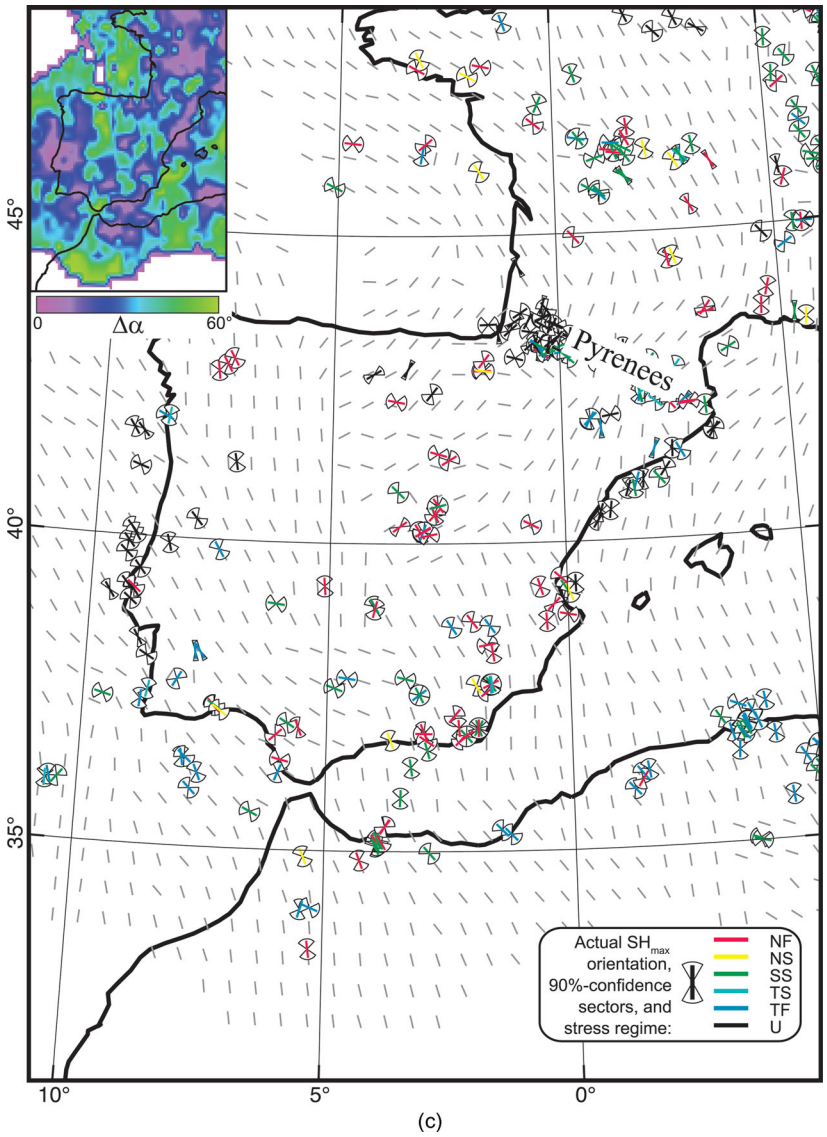

Figure 8. (*Continued.*)

and Hellenic Arc. As we move from the extension of the Apennines to the compression of the eastern coastline, the S_{Hmax} orientations rotate by 90° within a few tens of kilometres and turn perpendicular to the External Apennines thrust faults (Scrocca 2006; Basili & Barba 2007; Carafa & Barba 2011). Along the Hellenic Arc, similar transitions from extension to compression and subsequent abrupt reorientation of stresses occur in the Central Epirus (Northern Hellenides) and in the shallow marine zone between the Ionian Islands and mainland Greece (in the Southern Hellenides; Papanikolaou & Royden 2007; Jolivet *et al.* 2009; Papanikolaou *et al.* 2011).

4 VALIDATION

Independent validation is required to understand the degree to which the modelled stress field represents genuine features in Earth's crust. We performed two comparisons: one with synthetic data and one with similar studies available in the literature.

We ran a synthetic checkerboard test to evaluate the significance of short-wavelength stress patterns. The *a priori* stress flow lines were arranged in 110-km squares, with the stress patterns perpendicular to each other in adjacent squares. S_{Hmax} orientations were assigned to points at 0.2° intervals (Fig. 9). This synthetic data distribution corresponds to a data density of 2.05×10^{-3} data km^{-2}. To produce three additional synthetic data sets, S_{Hmax} orientations were randomly chosen with assumed data densities of 1.21×10^{-3}, 0.81×10^{-3}, and 0.37×10^{-3} data km^{-2}. These values are typical of the WSM08 data densities for much of Europe (Fig. 1), whereas the dimension of the squares and perpendicular S_{Hmax} orientations represent possible stress targets. We applied the interpolation procedure described in the previous section to each of the four data sets (one equispaced and three generated randomly) using the same threshold values ($N_{\mathrm{C}} \geq 3$, $\Delta\alpha < 60°$, and $\theta < 2.94°$) and a spacing of 0.2°. To quantify the agreement between the *a priori* and recovered checkerboards, we defined a correlation index as the fraction of the recovered S_{Hmax} orientations differing by less than 5° from the initial orientation. As expected,

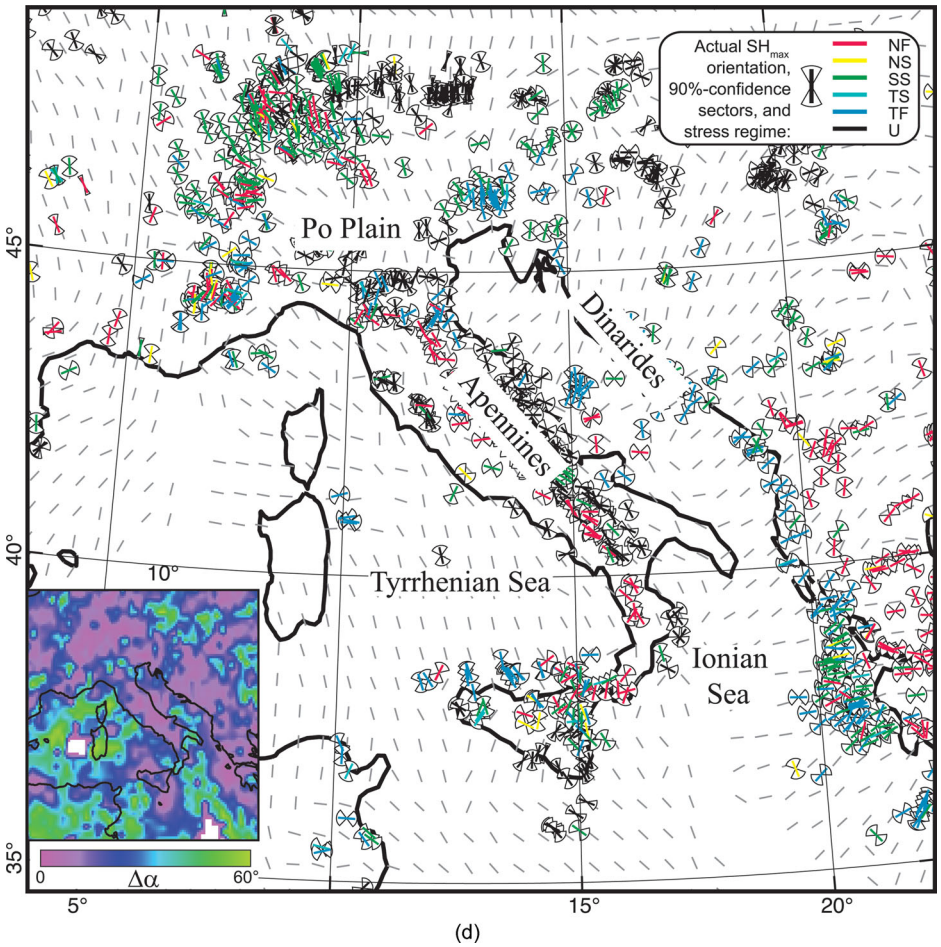

Figure 8. (*Continued.*)

the checkerboard was fully recovered (correlation index equal to one) for the equispaced synthetic data set (2.05×10^{-3} data km^{-2}). For the three random data sets, the correlation indices were 0.93 (for 1.21×10^{-3} data km^{-2}), 0.82 (for 0.81×10^{-3} data km^{-2}), and 0.70 (for 0.37×10^{-3} data km^{-2}). The stress patterns were satisfactorily recovered, both visually (Fig. 10) and according to the correlation index. This test demonstrates that our interpolation procedure can resolve the short-wavelength stress pattern in the parts of Europe with data densities similar to those considered here. In areas with very low data densities (such as Scandinavia and Northern Africa), the S_{Hmax} orientations represent the regional trend and can only be determined using longer ranges (Annulus $n = 6 - 8$, $2.05^\circ < \theta < 2.94^\circ$).

To compare our results with those obtained in similar studies in the literature, we selected the works of Heidbach *et al.* (2010) and Pierdominici & Heidbach (2012). We also applied the Bird & Li (1996) procedure (with pre-averaging and using the Bird & Li (1996) empirical two-point conditional probabilities calculated in WSM92) to WSM08 data. The S_{Hmax} orientations obtained with our method are significantly closer to those of Heidbach *et al.* (2010) than to those obtained by applying the method of Bird & Li (1996) to WSM08 (Fig. 11). This difference arises partly from the algorithm—the range cut-off was $\theta = 22^\circ$ for the global modelling of Bird & Li (1996) versus $\theta = 2.94^\circ$ in our case—and partly from the new set of conditional probabilities based on WSM08. Given the number of data points, the number of unique pairs in WSM08 is eight times larger than that in WSM92. This increase in the number of data pairs permits the investigation of shorter ranges and the resolution of greater spatial detail than in Bird & Li (1996). The S_{Hmax} orientations presented in this work are in good agreement with those from Heidbach *et al.* (2010) for Europe (Fig. 12). The criteria used in the smoothing procedure of Heidbach *et al.* (2010) requires more than five data points to be within a specified search radius and for the standard deviation of these data to be less than 25°. The search radius is initialised at 1000 km and decreased in 50-km steps until the standard deviation of the $N \geq 5 S_{\mathrm{Hmax}}$ orientations is less than 25°. Our approach and that presented in Heidbach *et al.* (2010) are both capable of determining the S_{Hmax} orientations for a large part of Europe; our results and theirs overlap by 28 per cent. Within this overlapping region, approximately 10 per cent of the S_{Hmax} orientations (corresponding to 3 per cent of the study area) differ by more than 25°, that is, more than the standard deviation of Heidbach *et al.* (2010). Approximately 3 per cent of the orientations (corresponding to 1 per cent of the study area) differ by more than 45°, indicating a lack of correlation (Fig. 12), which requires further investigation. Fig. 12 shows the area where the discrepancy in the S_{Hmax} orientations exceeds 25°. Most of these zones (Northeastern Iberia, the Western Alps, the Po Plain, the Northern Apennines, the Southern Tyrrhenian and Cyprus) are characterised by high data densities (greater than 1.2×10^{-3} data km^{-2}) and

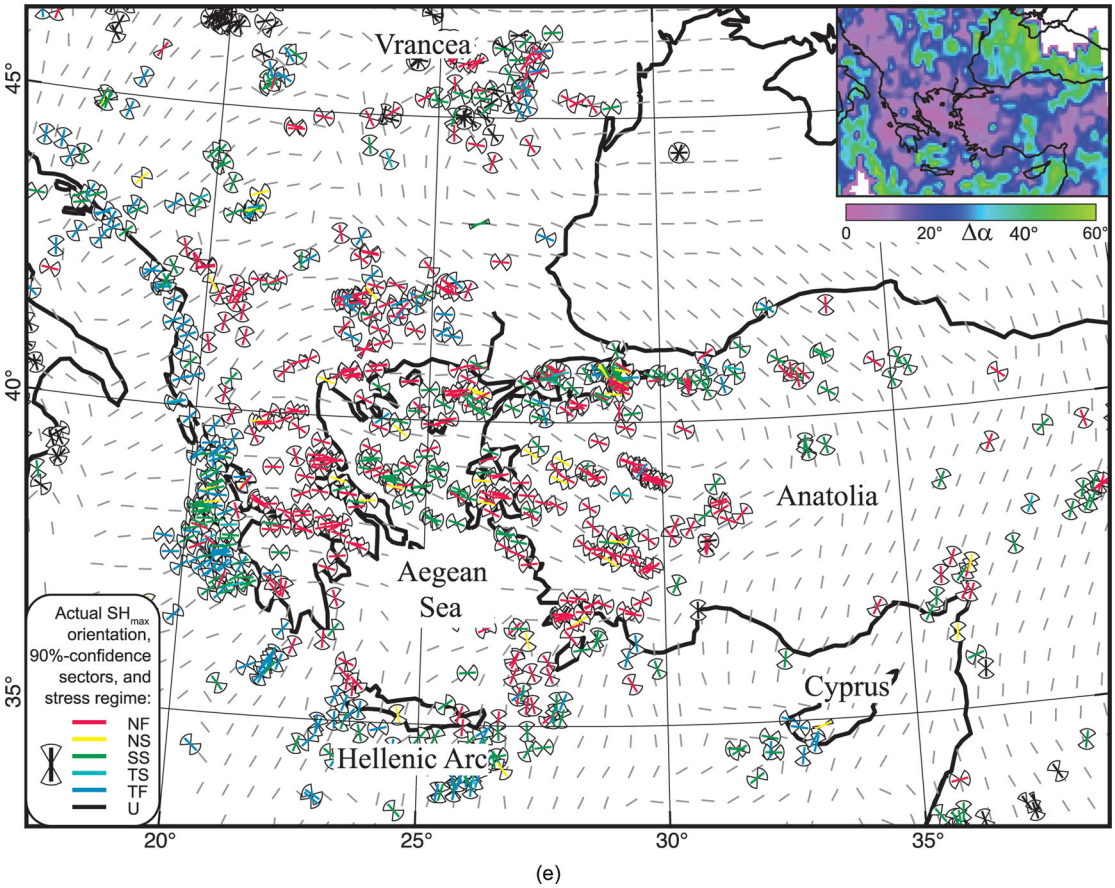

Figure 8. (*Continued.*)

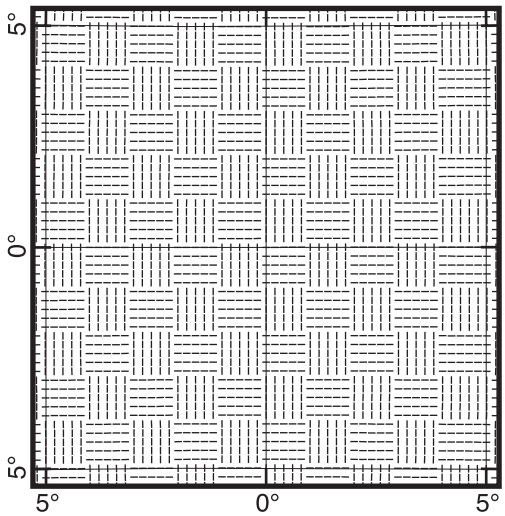

Figure 9. Input synthetic checkerboard stress orientations.

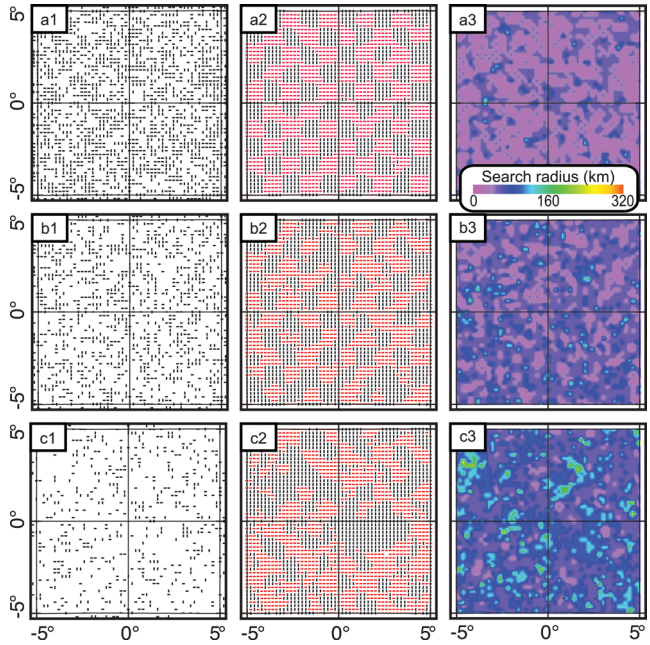

Figure 10. Results of the checkerboard test. From left to right: (1's) S_{Hmax} orientations randomly selected from the checkerboard shown in Fig. 9; (2's) interpolated stress field with the same threshold values used to calculate the S_{Hmax} orientations in Europe ($N_{\mathrm{C}} \geq 3$, $\Delta\alpha < 60°$, $\theta < 2.94°$); (3's) minimum search radius. From top to down: (a's) Data density of 1.21×10^{-3} data km^{-2}; (b's) data density of 0.81×10^{-3} data km^{-2}; (c's) data density of 0.37×10^{-3} data km^{-2}.

have short-wavelength stress sources and sharply rotating S_{Hmax} orientations, as described in the previous section. Based on these findings, we conclude that our method highlights the presence of short-wavelength stress patterns and sudden S_{Hmax} reorientations ($\theta < 100$ km) that cannot be identified with the minimum search radius of 100 km used in Heidbach *et al.* (2010).

To further validate our method and underline the importance of both pre-averaging the data and investigating short-range stress

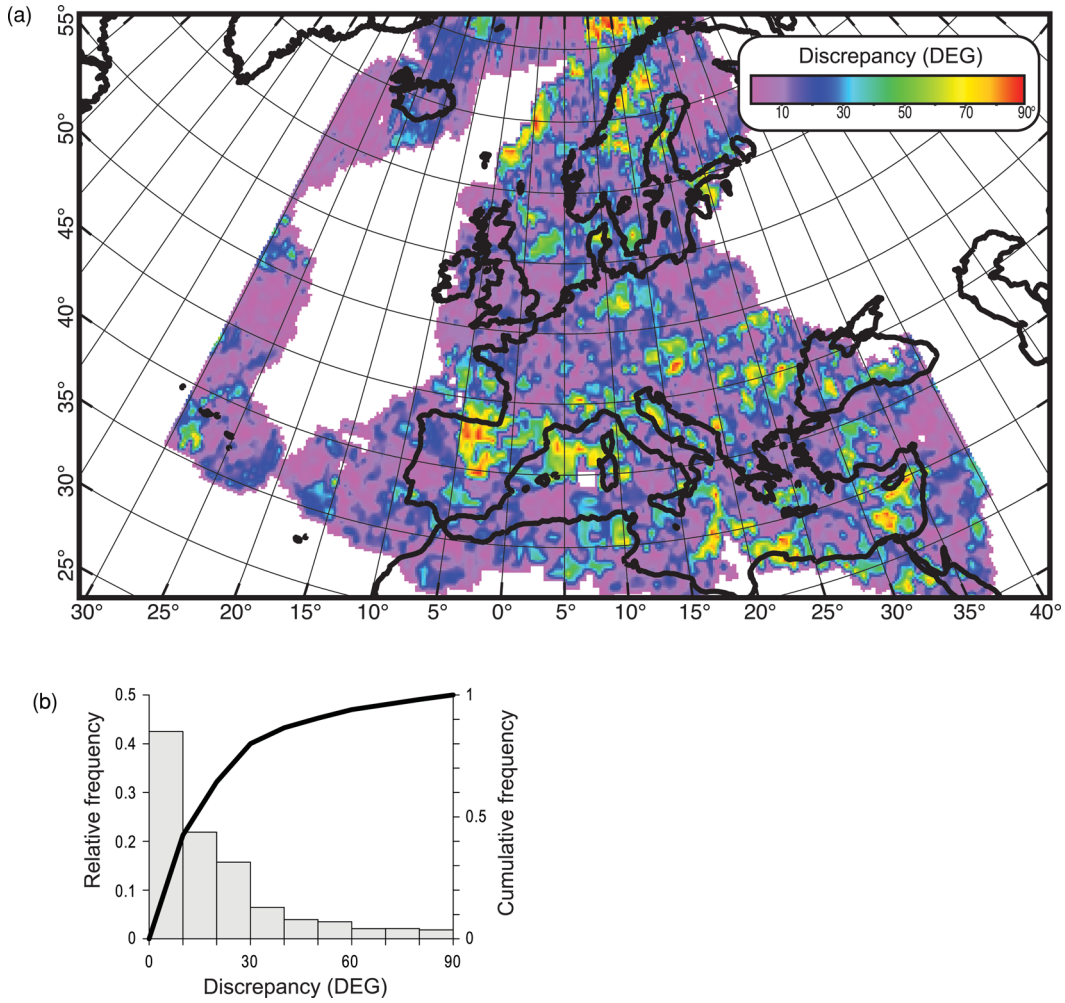

Figure 11. (a) Discrepancies between the S_{Hmax} stress orientations presented in this work and those obtained using the WSM08 and the probability distributions of Bird & Li (1996). The values are calculated on the Heidbach *et al.* (2010) grid. (b) Frequency distributions of the discrepancies (grey histogram: relative frequency; black line: cumulative frequency).

sources, we compared our results with those of Pierdominici & Heidbach (2012), in which the search radius was decreased from 1000 km to 100 km in 50-km steps. Their smoothing algorithm requires that more than 10 data points are located in at least two diagonal quadrants of the search circle around the grid point. The two methods display a good overall agreement, with the largest discrepancies in the S_{Hmax} orientations occurring in the Western Alps, Po Plain, Northern Apennines, Central Adriatic and Southern Tyrrhenian. These zones, characterised by high WSM08 data densities, are the same as those with large discrepancies between our work and that of Heidbach *et al.* (2010) (Fig. 13). We argue that our method performs better in terms of reproducing local patterns and sharp S_{Hmax} rotations, both of which are typical of these high-discrepancy zones.

5 DISCUSSION AND CONCLUSIONS

The method proposed here is appropriate for detecting short-wavelength patterns in S_{Hmax} orientations for large parts of Europe. Our use of analytical probabilities strengthens the contribution of the data close to the interpolation point, where fewer data are available. The data with superior quality factors (A, B and C) were included, while those with inferior quality factors (D and E) were omitted, which overcomes the difficulties of introducing a weighting scheme into the declustering algorithm.

Müller *et al.* (2003) suggested a search radius between 60 and 200 km for local stress field investigations. We have shown that for data densities greater than 0.8×10^{-3} data km^{-2}, reliable results can be obtained by pre-averaging the clustered data and choosing a search radius below 60 km (upper limit of Annulus $n = 2$; $\theta_2 < 0.52^{\circ}$, 58 km). In fact, a few independent data located at short distances tend to highlight local stress sources, whereas a large number of stress data (with a low standard deviation) at greater distances can dominate over the local stress. Increasing the distance increases the likelihood of mixing data affected by different sources of stress. In a few cases, the large number of distant and clustered data could counterbalance the distance weighting. Thus, the orientations of S_{Hmax} could be influenced more by the stress source sampled by the most data than by the local source of stress closest to the interpolation point.

We discuss two examples in which changes in the tectonic regime and rotations in stress orientations occur over short distances and the

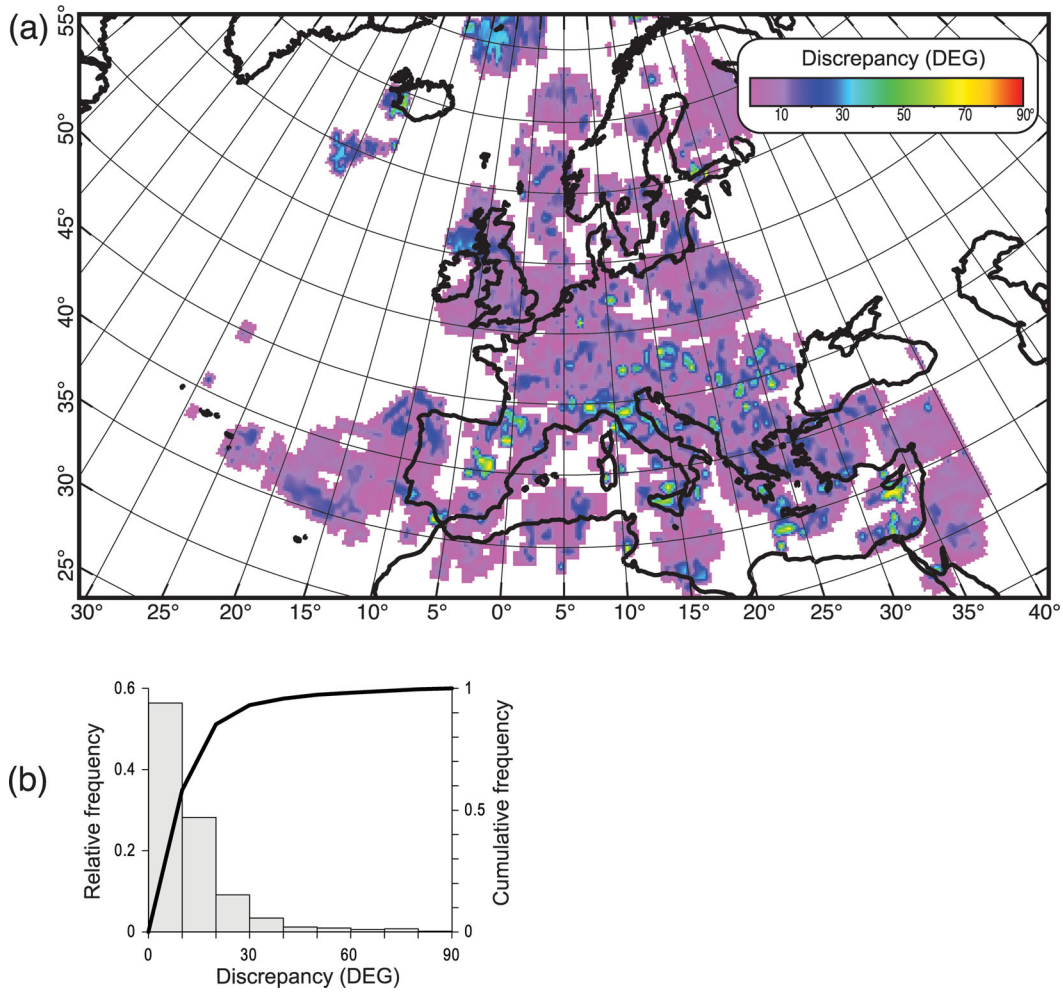

Figure 12. (a) Discrepancies between the S_{Hmax} orientations presented in this work and those of Heidbach *et al.* (2010). The values are calculated on the Heidbach *et al.* (2010) grid. (b) Frequency distributions of the discrepancies (grey histogram: relative frequency; black line: cumulative frequency).

S_{Hmax} orientations presented here differ from those reported in other studies (Heidbach *et al.* 2010; Pierdominici & Heidbach 2012). The first example (Fig. 14) is the transition from the NW–SE-oriented S_{Hmax} field caused by the extension in the Central Apennines (Bennett *et al.* 2012) to the NE–SW offshore compression of the Apenninic outer thrust (Boncio & Bracone 2009; Maesano *et al.* 2013). When a large search radius is considered (e.g. 100 km), the clustered stress data in the Central Apennines (80 per cent of the data) dominate the stress interpolation along the Adriatic coastline, causing S_{Hmax} to be parallel to the Marche coastline. In our interpolation scheme, 17 WSM08 data are declustered into 12 independent data, or clusters. The search radius for the interpolation point P_m (Fig. 14) is 24 km (corresponding to Annuli 1 and 2). Similar considerations also apply to the second example, concerning the Southern Tyrrhenian (Fig. 15). Moving from west to east, the S_{Hmax} field rotates from NW–SE, related to the Southern Tyrrhenian compression (Giunta *et al.* 2004), to NE-SW in the Peloritani area, which is undergoing extension. Between these two zones lies the Madonie-Nebrodi area, which is characterised by a NW–SE S_{Hmax} (Sgroi *et al.* 2012; Palano *et al.* 2012) that can only be detected with a search radius of less than 60 km. This area is also characterised by a high data density (greater than 0.8×10^{-3} data km^{-2}), and the search radius for the interpolation point P_s (Fig. 15) is 24 km for the three WSM08 data (which are independent data). In this case, a search radius of 100 km (as in Pierdominici & Heidbach 2012) captures data primarily related to the Peloritani extension, which is spread over the eastern part of the search area, and results in a different orientation than obtained when using a smaller search radius.

These examples demonstrate that the quantity of data available in WSM08 can be exploited with analytical probabilities by applying a declustering algorithm before interpolating and smoothing the data over a distance less than 60 km from the interpolation point. With future increases in the number of stress data, this approach will help to identify short-wavelength stress patterns and locate shifts in the S_{Hmax} orientations with higher spatial accuracy.

The distance weighting is a key component in the interpolation or smoothing of the data. The various algorithms differ in the weighting function used (see Introduction and Fig. 16 for a comparison). In this work, we used exponentials, which provide high-quality fits to the empirical discrepancy-range relations for the WSM08 data. For the data located near an interpolation point, Heidbach *et al.* (2010) adopted an inverse distance weighting that produces the maximum weight among the methods reviewed in this paper. Bird & Li (1996) employed a more uniform weight at small distances due to the scarcity of data in WSM92. The development of WSM08 (Zang *et al.* 2012), other available data, and new empirical probabilities

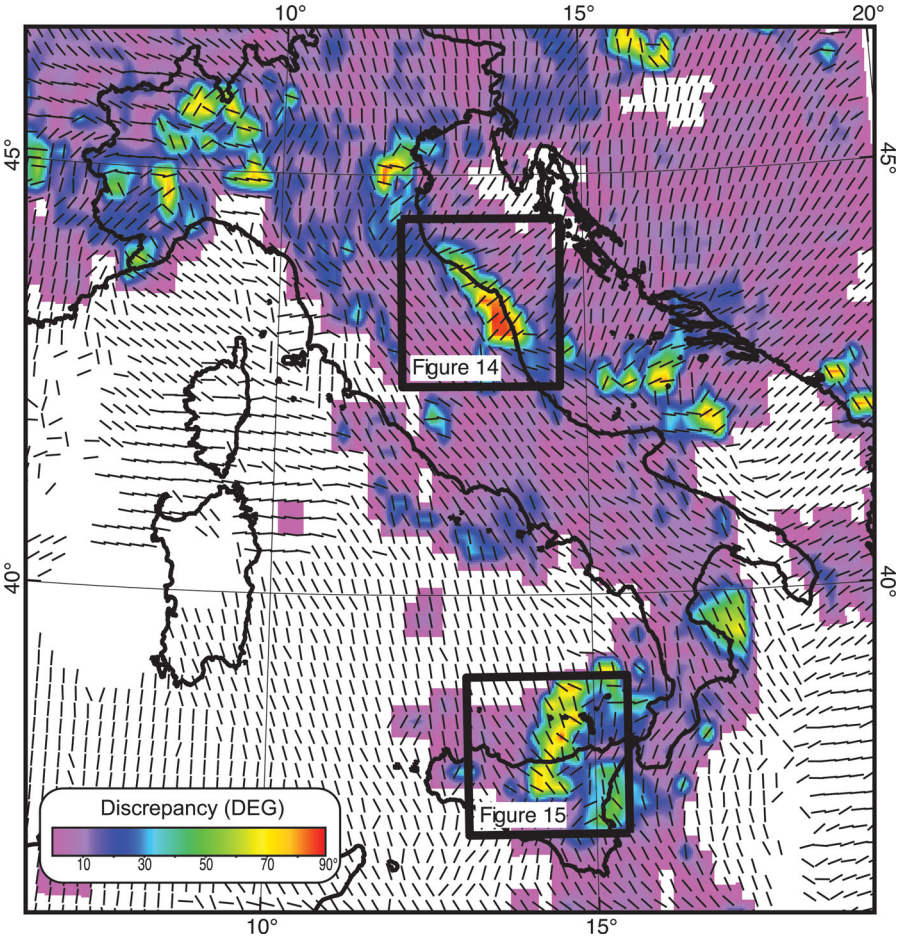

Figure 13. Interpolated S_{Hmax} orientations in Italy, calculated on the Pierdominici & Heidbach (2012) grid. The colours indicate the discrepancies between the S_{Hmax} orientations obtained using the algorithm presented here and the orientations of Pierdominici & Heidbach (2012). The rectangles indicate the areas shown in Figs 14 and 15.

will permit further assessment of the quality of the various distance-weighting schemes.

The approach presented here can be used to estimate fault activity through kinematic or dynamic models and to predict the stress orientations of future earthquakes, for example, for seismic hazard assessment, even where instrumental earthquake recordings are unavailable. Interestingly, several mountain ranges exhibit 90° rotations of the S_{Hmax} orientation from their crests (which are often in horizontal tension and experience normal faulting) to their foothills (which often undergo thrust faulting). This pattern, seen in the Pyrenees, Alps, Southern Scandes, Hellenic Arc and Apennines, places a strong constraint on the magnitude of the tectonic stresses with respect to the topographic load, a matter that has often debated (e.g. Bird 1998; Bird *et al.* 2008). Varying topograpical loads are known to produce stress magnitudes of up to 20–30 MPa, which significantly influences the stress orientations. This influence occurs not only in continental Europe (Gölke & Coblentz 1996), where tectonic stresses are very small, but also in the Alpine-Dinaric belt and Pannonian Basin, where 2-km changes in elevation generate tensional stresses ranging from 6 to 22 MPa in the mountain belt and compressional stresses ranging from 3 to 12 MPa in the basin (Bada *et al.* 2001). Tectonic stresses are often estimated to be high at plate boundaries due to ridge push or sinking slabs (80–120 MPa; Whittaker *et al.* 1992), but these stresses are expected to produce observable shear heating (e.g. Molnar & England 1990). However, the influence of these stresses within continents remains controversial. In fact, stresses on major faults have been found to be smaller than 30 MPa (e.g. Mount & Suppe 1987; Zoback *et al.* 1987), and basal tractions acting across continents have been estimated to produce changes of up to 20 MPa in compressive stresses (e.g. Bird 1998; Ghosh *et al.* 2008). The 90° rotation of the S_{Hmax} suggests that, at least in the mountain ranges where these rotations are observed, the magnitude of tectonic and topographic stress must be comparable, thus supporting the hypothesis that tectonic stresses can be characterized by relatively low magnitudes of 20–30 MPa. As an indirect consequence, this finding supports the idea that topographic stress can cause an inversion, at a certain depth, of the expected pattern of differential stress, allowing for the initiation of ruptures on low-angle thrust faults at shallow depths to propagate downward (Carminati *et al.* 2004).

The derived S_{Hmax} orientations describe the present-day stress field in Europe. The proposed approach produced acceptable uncertainties for nearly half of Europe. The modified Bird & Li (1996) algorithm facilitates the identification of third-order features, such as topography effects and crustal-scale density heterogeneities. The stress orientations modelled in this work are generally compatible

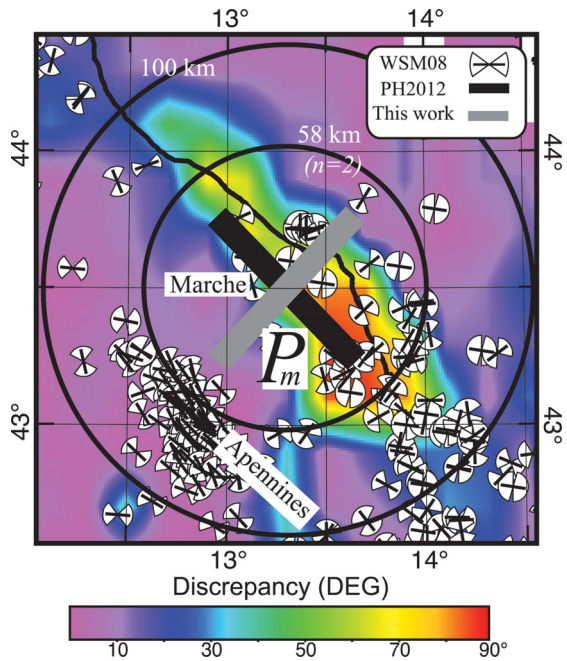

Figure 14. Comparison of the S_{Hmax} orientation obtained using our algorithm with that obtained by Pierdominici & Heidbach (2012) for the external Apennines. See Fig. 13 for the location of the area. Thick black bar (PH2012): smoothed S_{Hmax} orientation calculated by Pierdominici & Heidbach (2012) with a search radius of 100 km; thick grey bar: interpolated S_{Hmax} orientation obtained in the present work ($N_{\mathrm{C}} = 12$; search radius $\theta = 0.52^{\circ}$, 58 km); P_m: interpolation point. The background colours indicate the discrepancies between the S_{Hmax} orientations obtained using the algorithm presented here and those of Pierdominici & Heidbach (2012). The multicolour lines denote the S_{Hmax} orientations for different kinematic regimes (WSM08; Heidbach *et al.* 2008). Tectonic regime identifiers: NF, normal fault; NS, normal-oblique; SS, strike-slip; TS, thrust-oblique; TF, thrust; U, unknown tectonic regime.

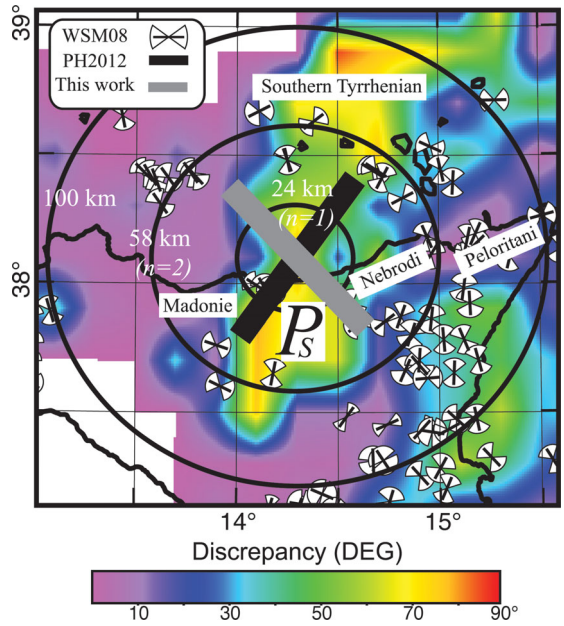

Figure 15. Comparison of the S_{Hmax} orientation obtained using our algorithm ($N_{\mathrm{C}} = 13$; search radius $\theta = 0.52^{\circ}$, 58 km; P_s: interpolation point) with that obtained by Pierdominici & Heidbach (2012) for Northern Sicily. See Fig. 13 for the location of the area and the caption of Fig. 14 for further explanations.

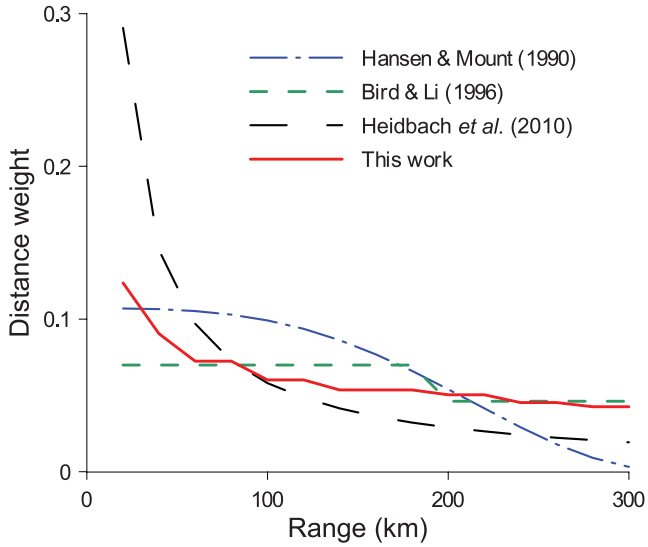

Figure 16. Normalised distance weight of different algorithms for points at distances between 20 and 340 km with 20-km steps. See Hansen & Mount 1990; Bird & Li 1996; Heidbach *et al.* 2010.

with those of previous studies. However, for areas with data densities greater than 0.8×10^{-3} data km^{-2}, our algorithm outperforms the existing methods in identifying short-wavelength stress sources.

ACKNOWLEDGMENTS

We thank the associate editor Saskia Goes, Peter Bird and John Townend for their thorough reviews. We thank D. Coblentz for his valuable comments on an early version of the manuscript, S. Pierdominici for kindly supplying the results of her work, O. Heidbach for suggesting that we perform synthetic tests and again P. Bird for the NeoKinema.f90 code, which helped us to design our work. This work was supported by the DPC-INGV 2008–2010 S1 project, the EU-FP7 project 'Seismic Hazard Harmonization in Europe' (SHARE; Grant agreement no. 226967), and project MIUR-FIRB 'Abruzzo' (code: RBAP10ZC8K_003). Some figures were created using Generic Mapping Tools (Wessel & Smith 1998).

REFERENCES

Amante, C. & Eakins, B.W., 2009. ETOPO1 1 Arc-Minute Global Relief Model: Procedures, Data Sources and Analysis. NOAA Technical Memorandum NESDIS NGDC-24, 19 pp.

Andeweg, B., De Vicente, G., Cloetingh, S., Giner, J. & Muñoz Martin, A., 1999. Local stress fields and intraplate deformation of Iberia: variations in spatial and temporal interplay of regional stress sources, *Tectonophysics,* **305,** 153–164.

Arnold, R. & Townend, J., 2007. A Bayesian approach to estimating tectonic stress from seismological data, *Geophys. J. Int.,* **170,** 1336–1356.

Assameur, D.M. & Mareschal, J.-C., 1995. Stress induced by topography and crustal density heterogeneities: implication for the seismicity of southeastern Canada, *Tectonophysics,* **241**(3–4), 179–192.

Bada, G., Horvath, F., Cloetingh, S. & Coblentz, D.D., 2001. Role of topography-induced gravitational stresses in basin inversion: the case study of the Pannonian basin, *Tectonics,* **20,** 343–363.

Barba, S., Carafa, M.M.C., Mariucci, M.T., Montone, P. & Pierdominici, S., 2010. Present-day stress field modelling of southern Italy constraining by stress and GPS data, *Tectonophysics,* **482**(1–4), 193–204.

Barba, S., Finocchio, D., Sikdar, E. & Burrato, P., 2013. Modeling the interseismic deformation of a thrust system: seismogenic potential of the Southern Alps, Terra Nova, in press, doi:10.1111/ter.12026.

Basili, R. & Barba, S., 2007. Migration and shortening rates in the Northern Apennines, Italy: implications for seismic hazard, *Terra Nova,* **19**(6), 462–468.

Bennett, R.A. *et al.*, 2012. Syn-convergent extension observed using the RETREAT GPS network, northern Apennines, Italy, *J. geophys. Res.,* **117,** B04408, doi:10.1029/2011JB008744.

Bird, P. & Li, Y., 1996. Interpolation of principal stress directions by non-parametric statistics: global maps with confidence limits, *J. geophys. Res.,* **101**(B3), 5435–5443.

Bird, P., 1998. Testing hypotheses on plate-driving mechanisms with global lithosphere models including topography, thermal structure, and faults, *J. geophys. Res.,* **103**(B5), 10 115–10 129.

Bird, P., Liu, Z. & Rucker, W.K., 2008. Stresses that drive the plates from below: definitions, computational path, model optimization, and error analysis, *J. geophys. Res.,* **113**(B11406), 1–32.

Boncio, P. & Lavecchia, G., 2000. A structural model for active extension in central Italy, *J. Geodyn.,* **29,** 233–244.

Boncio, P. & Bracone, V., 2009. Active stress from earthquake focal mechanisms along the Padan-Adriatic side of the Northern Apennines (Italy), with considerations on stress magnitudes and pore-ffiuid pressures, *Tectonophysics,* **476**(1–2), 180–194.

Bungum, H., Olesen, O., Pascal, P., Gibbons, S., Lindholm, C. & Vestøl, O., 2010. To what extent is the present day seismicity in Norway driven by post-glacial rebound? *J. Geol. Soc., Lond*, **167,** 373–384.

Caporali, A., Barba, S., Carafa, M.M.C., Devoti, R., Pietrantonio, G. & Riguzzi, F., 2011. Static stress drop as determined from geodetic strain rates and statistical seismicity, *J. geophys. Res.,* **116,** B02410.

Carafa, M.M.C. & Barba, S., 2011. Determining rheology from deformation data: the case of central Italy, *Tectonics,* **30,** TC2003.

Carminati, E., Doglioni, C. & Barba, S., 2004. Reverse migration of seismicity along thrusts and normal faults, *Earth-Sci. Rev.,* **65**(3–4), 195–222.

Carminati, E. & Vadacca, L., 2010. Two- and three-dimensional numerical simulations of the stress field at the thrust-front of the Northern Apennines, Italy, *J. geophys. Res.,* **115,** B12425.

Carminati, E., Scrocca, D. & Doglioni, C., 2010. Compaction-induced stress variations with depth in an active anticline: Northern Apennines, Italy, *J. geophys. Res.,* **115,** B02401.

Carminati, E., Toniolo Augier, F. & Barba, S., 2001. Dynamic modeling of stress accumulation in central Italy: role of structural heterogeneities and rheology, *Geophys. J. Int.,* **144,** 373–390.

Coblentz, D.D. & Richardson, R.M., 1995. Statistical trends in the intraplate stress field, *J. geophys. Res.,* **100**(20), 245–255.

Decker, K., Meschede, M. & Ring, U., 1993. Fault slip analysis along the northern margin of the Eastern Alps (Mollasse, Helvethic nappes, North- and South-Penninic ffiysch and the Northern Calcareous Alps), *Tectonophysics,* **223,** 291–312.

De Vicente, G., Giner, J.L., Munoz Martin, A., Gonzalez-Casado, J.M. & Lindo, R., 1996. Determination of present-day stress tensor and neotectonic interval in the Spanish Central System and Madrid Basin, central Spain, *Tectonophysics,* **266,** 405–424.

Geletti, R., Del Ben, A., Busetti, M., Ramella, R. & Volpi, V., 2008. Gas seeps linked to salt structures in the Central Adriatic Sea, *Basin Res.,* **20,** 473–487.

Ghosh, A., Holt, W.E., Wen, L., Haines, A.J. & Flesch, L.M., 2008. Joint modeling of lithosphere and mantle dynamics elucidating lithosphere-mantle coupling, *Geophys. Res. Lett.,* **35**(L16309), 1–5.

Grandić, S. & Markulin, Ž., 2000. Triassic synrift euxinic basins as a factor of exploration risk in the Croatian offshore area, in *Proceedings of International Symposium of Petroleum Geology*, April 22–24, 1999, Nafta (Zagreb, Croatia), 51(spec. issue), pp. 41–50.

Goes, S., Loohuis, J.J.P., Wortel, M.J.R. & Govers, R., 2000. The effect of plate stresses and shallow mantle temperatures on tectonics of northwestern Europe, *Global Planet. Change,* **27,** 23–39.

Gölke, M. & Coblentz, D., 1996. Origins of the European regional stress field, *Tectonophysics,* **266,** 11–24.

Ghisetti, F.C. & Sibson, R.H., 2012. Compressional reactivation of E–W inherited normal faults in the area of the 2010–2011 Canterbury earthquake sequence, *N. Z. J. Geol. Geophys.,* **55**(3), 177–184.

Giunta, G. *et al.*, 2004. The Palermo (Sicily) seismic cluster of September 2002, in the seismotectonic framework of the Tyrrhenian Sea–Sicily border area, *Ann. Geophys.,* **47**(6), 1755–1770.

Hansen, K.M. & Mount, V.S., 1990. Smoothing and extrapolation of crustal stress orientation measurements, *J. geophys. Res.,* **95**(B2), 1155–1165.

Hardebeck, J.L. & Michael, A.J., 2006. Damped regional-scale stress inversions: methodology and examples for southern California and the Coalinga aftershock sequence, *J. geophys. Res.,* **111,** B11310, doi:10.1029/2005JB004144.

Heidbach, O., Tingay, M., Barth, A., Reinecker, J., Kurfeß, D. & Müller, B., 2008. doi:10.1594/GFZ.WSM.Rel2008. Last accessed date: February 8, 2013.

Heidbach, O., Tingay, M., Barth, A., Reinecker, J., Kurfeß, D. & Müller, B., 2010. Global crustal stress pattern based on the World Stress Map database release 2008, *Tectonophysics,* **482,** 3–15.

Hergert, T. & Heidbach, O., 2011. Geomechanical model of the Marmara Sea region — II. 3-D contemporary background stress field, *Geophys. J. Int.,* **185**(3), 1090–1102.

Herraiz, M. *et al.*, 2000. The recent (upper Miocene to Quaternary) and present tectonic stress distributions in the Iberian Peninsula, *Tectonics,* **19**(4), 762–786.

Herrmann, R.B., Malagnini, L. & Munafo, I., 2011. Regional moment tensors of the 2009 L'Aquila earthquake sequence, *Bull. seism. Soc. Am.,* **101,** 975–993.

Kastelic, V. & Carafa, M.M.C., 2012. Fault slip rates for the active External Dinarides thrust-and-fold belt, *Tectonics,* **31,** TC3019.

Korbar, T., 2009. Orogenic evolution of the External Dinarides in the NE Adriatic region: a model constrained by tectonostratigraphy of Upper Cretaceous to Paleogene carbonates, *Earth Sci. Rev.,* **96**(4), 296–312.

Jolivet, L., Faccenna, C. & Piromallo, C., 2009. From mantle to crust: stretching the Mediterranean, *Earth planet. Sci. Lett.,* **285,** 198–209.

Lee, J.C. & Angelier, J., 1994. Paleostress trajectory maps based on the results of local determinations: the "Lissage" program, *Comput. Geosci.,* **20,** 161–191.

Liesa, C.L. & Simón, J.L., 2009. Evolution of intraplate stress fields under multiple remote compressions: the case of the Iberian Chain (NE Spain), *Tectonophysics,* **474**(1–2), 144–159.

Lund, B. & Townend, J., 2007. Calculating horizontal stress orientations with full or partial knowledge of the tectonic stress tensor, *Geophys. J. Int.,* **170**(3), 1328–1335.

Maesano, F.E., Toscani, G., Burrato, P., Mirabella, F., D'Ambrogi, C. & Basili, R., 2013. Deriving thrust fault slip rates from geological modeling: examples from the Marche coastal and offshore contraction belt, Northern Apennines, Italy, *Mar. Petrol. Geol.,* in press, doi:10.1016/j.marpetgeo.2012.10.008.

Mardia, K.V., 1972. *Statistics of Directional Data: Probability and Mathematical Statistics,* Academic Press, London, 357 pp.

Molnar, P. & England, P., 1990. Temperatures, heat flux, and frictional stress near major thrust faults, *J. geophys. Res.,* **95**(B4), 4833–4856.

Mount, V.S. & Suppe, J., 1987. State of stress near the San Andreas fault: implications for wrench tectonics, *Geology,* **15,** 1143–1146.

Müller, B., Heidbach, O., Negut, M., Sperner, B. & Buchmann, T., 2010. Attached or not attached—evidence from crustal stress observations for a weak coupling of the Vrancea slab in Romania, *Tectonophysics,* **482**(1–4), 139–149.

Müller, B., Wehrle, V., Hettel, S., Sperner, B. & Fuchs, K., 2003. A new method for smoothing orientated data and its application to stress data, in *Fracture and In-Situ Stress Characterization of Hydrocarbon Reservoirs,* Vol. 209, pp. 107–126, ed. Ameen, M.S., Geol. Soc. Lond. Spec. Publ.

Müller, B., Wehrle, V., Zeyen, H.J. & Fuchs, K., 1997. Short-scale variations of tectonic regimes in the western European stress province north of the Alps and Pyrenees, *Tectonophysics,* **275,** 199–219.

Müller, B., Zoback, M.L., Fuchs, K., Mastin, L., Gregersen, S., Pavoni, N., Stephansson, O. & Ljunggren, C., 1992. Regional patterns of tectonic stress in Europe, *J. geophys. Res.,* **97,** 11 783–11 803.

Palano, M., Ferranti, L., Monaco, C., Mattia, M., Aloisi, M., Bruno, V., Cannavò, F. & Siligato, G., 2012. GPS velocity and strain fields in Sicily and southern Calabria, Italy: updated geodetic constraints on tectonic block interaction in the central Mediterranean, *J. geophys. Res.,* **117,** B07401, doi:10.1029/2012JB009254.

Papanikolaou, D. & Royden, L., 2007. Disruption of the Hellenic arc: late Miocene extensional detachment faults and steep Pliocene-Quaternary normal faults—Or what happened at Corinth? *Tectonics,* **26,** TC5003, doi:10.1029/2006TC002007.

Papanikolaou, D., Royden, L. & Vassilakis, E., 2011. Neotectonic and active diverging rates of extension in the northern and southern Hellenides across the central Hellenic shear zone, in *INQUA-IGCP 567 Proceedings, Vol. 2, Edited by INQUA-TERPRO Focus Area on Paleoseismology and Active Tectonics & IGCP-567 Earthquake Archaeology*, Greece, ISBN 978–960-466–093-3.

Pascal, C. & Cloetingh, S.A.P.L., 2009. Gravitational potential stresses and stress field of passive continental margins: insights from the south Norway shelf, *Earth planet. Sci. Lett.,* **277,** 464–473.

Petricca, P., Carafa, M.M.C., Barba, S. & Carminati, E., 2013. Local, regional, and plate scale sources for the stress field in the Adriatic and Periadriatic region, *Mar. Petrol. Geol.,* in press, doi:10.1016/j.marpetgeo.2012.08.005.

Pierdominici, S. & Heidbach, O., 2012. Stress field of Italy—mean stress orientation at different depths and wave-length of the stress pattern, *Tectonophysics,* **532–535,** 301–311.

Rebai, S., Herve, P. & Taboada, A., 1992. Modern tectonic stress field in the Mediterranean region: evidence for variation in stress directions at different scales, *Geophys. J. Int.,* **110,** 106–140.

Scrocca, D., 2006. Thrust front segmentation induced by differential slab retreat in the Apennines (Italy), *Terra Nova,* **18,** 154–161.

Sgroi, T., de Nardis, R. & Lavecchia, G., 2012. Crustal structure and seismotectonics of central Sicily (southern Italy): new constraints from instrumental seismicity, *Geophys. J. Int.,* **189**(3), 1237–1252.

Sibson, R., Ghisetti, F. & Ristau, J., 2011. Stress control of an evolving strike-slip fault system during the 2010–2011 Canterbury, New Zealand, earthquake sequence, *Seismol. Res. Lett.,* **82,** 824–832.

Syracuse, E.M. *et al.*, 2012. Temporal and spatial evolution of hypocentres and anisotropy from the Darfield aftershock sequence: implications for fault geometry and age, *N. Z. J. Geol. Geophys.,* **55**(3), 287–293.

Sue, C., Delacou, B., Champagnac, J.D., Allanic, C., Tricart, P. & Burkhard, M., 2007. Extensional neotectonics around the bend of the Western/Central Alps: an overview, *Int. J. Earth Sci.,* **96,** 1101–1129.

Taymaz, T., Jackson, J. & McKenzie, D., 1991. Active tectonics of the north and central Aegean Sea, *Geophys. J. Int.,* **106,** 433–490.

Wessel, P. & Smith, W.H.F., 1998. New, improved version of the Generic Mapping Tools released, *EOS. Trans. Am. geophys. Un.,* **79,** 579.

Wdowinski, S., Ben-Avraham, Z., Arvidsson, R. & Ekstroem, G., 2006. Seismotectonics of the Cyprian Arc, *Geophys. J. Int.,* **164,** 176–181.

Whittaker, A., Bott, M.H.P. & Waghorn, G.D., 1992. Stresses and plate boundary forces associated with subduction plate margins, *J. geophys. Res.,* **97**(B8), 11 933–11 944.

Zang, A., Stephansson, O., Heidbach, O. & Janouschkowetz, S., 2012. World stress map database as a resource for rock mechanics and rock engineering, *Geotech. Geol. Eng.,* **30**(3), 625–646.

Zoback, M.D. *et al.*, 1987. New evidence on the state of stress of the San Andreas fault system, *Science,* **238,** 1105–1111.

Zoback, M.L., 1992. First and second order patterns of stress in the lithosphere: the World Stress Map Project, *J. geophys. Res.,* **97**(B8), 11 703–11 728.

SUPPORTING INFORMATION

Additional Supporting Information may be found in the online version of this article:

Figure S1. S_{Hmax} orientations in Europe with confidence limits. Red bars: interpolated orientations (this work); black bars: confidence limits (this work). Relief model from ETOPO1 (Amante & Eakins 2009).

Table S1. The interpolated stress orientations in Europe (330W-40E;25N-76N) (http://gji.oxfordjournals.org/lookup/supp1/doi:10.1093/gji/ggt024/-/DC1).

Please note: Oxford University Press is not responsible for the content or functionality of any supporting materials supplied by the authors. Any queries (other than missing material) should be directed to the corresponding author for the article.